CHALMERS
UNIVERSITY OF TECHNOLOGY

Prediction of long-term differential track settlement in a transition zone using an iterative approach

Engineering Structures 283 (2023) 115830

Contents lists available at ScienceDirect

Engineering Structures

journal homepage: www.elsevier.com/locate/engstruct

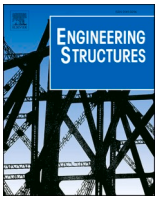

Prediction of long-term differential track settlement in a transition zone using an iterative approach

Kourosh Nasrollahi [a,*], Jens C.O. Nielsen [a], Emil Aggestam [b], Jelke Dijkstra [c], Magnus Ekh [d]

[a] Department of Mechanics and Maritime Sciences, Division of Dynamics/CHARMEC Chalmers University of Technology, SE-412 96 Gothenburg, Sweden
[b] Trafikverket, SE-411 04 Gothenburg, Sweden
[c] Department of Architecture and Civil Engineering Chalmers University of Technology, SE-412 96 Gothenburg, Sweden
[d] Department of Industrial and Materials Science Chalmers University of Technology, SE-412 96 Gothenburg, Sweden

ARTICLE INFO

Keywords:
Transition zone
Empirical settlement model
Dynamic vehicle–track interaction
Non-linear track model
Heavy haul traffic
Slab track
Under sleeper pads

ABSTRACT

A methodology for the simulation of long-term differential track settlement, the development of voided sleepers leading to a redistribution of rail seat loads, and the evolving irregularity in vertical track geometry at a transition between two track forms, is presented. For a prescribed traffic load, the accumulated settlement is predicted using an iterative approach. It is based on a time-domain model of vertical dynamic vehicle–track interaction to calculate the contact forces between sleepers and ballast in the short-term. These are used in an empirical model to determine the long-term settlement of the ballast/subgrade below each sleeper. Gravity loads and state-dependent track conditions are accounted for, including a prescribed variation of non-linear stiffness of the supporting foundation along the track model. In parallel, a two-dimensional (2D) non-linear finite element model of layered soil is verified versus field measurements and used to determine the support stiffness of each sleeper in the track model. The methodology is applied to a transition zone between a ballasted track and a slab track that is subjected to heavy haul traffic. Analyses of the influence of higher axle loads and the implementation of under sleeper pads on sleeper settlement are demonstrated.

1. Introduction

In transition zones between two different track forms, there is a discontinuity in track structure leading to a gradient in track stiffness. Examples include transitions between different superstructures, e.g., slab track to ballasted track [1], and/or between different substructures, e.g., embankment to a bridge or tunnel structure [2–5]. Differences in loading and support conditions at the interfaces between track superstructure and substructure on either side of the transition may lead to differential track settlement, voided sleepers, and an evolving irregularity in longitudinal level soon after construction. This results in an amplification of the dynamic traffic loading along the transition contributing to the degradation process of ballast and subgrade and resulting in a further deterioration of vertical track geometry. Hence, track adjacent to a transition is prone to deteriorate at an accelerating rate, and costly maintenance work to rectify the geometry and support conditions may be required on recurrent occasions [1,6–11].

Even though ballasted track is the most common track form, modern infrastructure for high-speed railway traffic is often built using slab track [1,12,13]. Compared to ballasted track, slab track has several advantages, e.g., higher lateral track resistance and eliminated problems with ballast degradation. This reduces the need for regular maintenance and extends service life. However, should maintenance work on slab track be required, it is often more costly compared to maintenance work on ballasted track. Furthermore, there is less tolerance for corrections compared to ballasted track. Over the years, the use of optimised and prefabricated slab track systems has increased, and the initial cost ratio compared to ballasted track has been reduced [14]. For example, the "Moulded Modular Multi-Blocks slab-track" (3 MB) concept is a reinforced standard precast slab designed for both mixed and high-speed traffic [14]. As part of the European Union's Horizon 2020 research and innovation programme in the projects In2Track2 and In2Track3, this particular design will be demonstrated in the field on a short section of track on the heavy haul line Malmbanan in Sweden with tests starting in autumn 2022.

To reduce the required maintenance work associated with transitions, various types of transition zone designs can be implemented. A key design idea is to reduce the stiffness gradient by making the softer

* Corresponding author.
E-mail address: Kourosh.nasrollahi@chalmers.se (K. Nasrollahi).

https://doi.org/10.1016/j.engstruct.2023.115830
Received 24 August 2022; Received in revised form 6 January 2023; Accepted 16 February 2023
Available online 28 February 2023

track stiffer and the stiffer track softer adjacent to the transition. Examples of solutions include applications of under sleeper pads (USPs), auxiliary rails, approach slab, varying sleeper length/width, etc., see the review by Sañudo et al. [6]. Another review by Indraratna et al. [10] discusses research work carried out using large-scale laboratory testing, field measurements in transition zones, as well as mathematical and computational modelling. Based on a three-dimensional (3D) finite element (FE) model that had been calibrated versus field measurements, Paixão et al. [9] investigated the influence of USPs and their layout along the transition zone on the dynamic behaviour of transition zones and the reduction of vertical stiffness gradient. Chumyen et al. [15] used a calibrated 3D FE model to study the influence of distance between the auxiliary rails, as well as soil improvement, on the dynamic characteristics of the transition zone. It was found that a wider distance between the auxiliary rails can improve the design, but the positive effect of soil stiffening was greater.

Long-term settlement of transition zones has been studied extensively in the literature. Two main approaches to model and predict track settlement have been suggested. One approach involves either a 3D FE (continuum scale) model, incorporating yield criteria, plastic flow rules, and hardening rules, or a discrete element (DE) model framework to simulate the local deformations and stresses in the substructure [16–20]. The alternative approach is using a simplified one-dimensional Winkler type model coupled with an empirical settlement formula as in Refs. [21,22]. Such empirical formulae are typically based on cyclic triaxial test data, reduced-scale models [23], or in situ measurements. Reviews of existing mechanistic-empirical settlement formulae can be found in Refs. [20,24]. In Ref. [25], empirical parameters for the prediction of subgrade settlement were obtained by conducting triaxial laboratory tests on different soils to investigate the plastic deformation under cyclic loading.

In several models, the settlement is calculated and extrapolated as a function of the logarithm of the number of load cycles. However, generally, these models do not account for the variation and redistribution of loads supporting the adjacent sleepers that occur over time due to accumulated differential settlement and the potential appearance of voided sleepers. Further, track irregularities evolve with each axle load passage as for each passing wheel, the dynamic wheel–rail contact force, the distribution of stresses within the different track layers, and the induced settlements might be different. Compared with using a constitutive model, results from empirical models have been reported to be similar in accuracy yet depending on a much smaller number of input parameters [26]. Constitutive models are often associated with a higher computational cost [27].

The stresses induced in the ballast and subgrade are a key input to both the constitutive and empirical settlement models. A common technique is to use an integrated approach where a model of the dynamic vehicle–track interaction in the short term is combined with an empirical model of the long-term settlement. For example, Sayeed and Shahin [28] considered the effect of a moving dynamic vehicle load when applying a 3D FE model to compute the deviatoric stresses in the foundation that were then used as input in an empirical settlement model. A cyclic domain model integrated with an iterative approach to compute differential track settlement accounting for longitudinal variations in load and track characteristics was developed by Li et al. [29].

By replacing the 3D FE model with a representative, discrete, state-dependent spring-damper model of the supporting foundation, simulation time can be reduced significantly. Nielsen and Li [22] used this approach to predict the deterioration of track geometry due to differential settlement adjacent to a rail joint. Wang and Markine [2] applied a 3D FE model of a transition zone in their simulations of dynamic vehicle–track interaction and stresses in the foundation, combined with an empirically-based 1D model to compute the resulting settlement per sleeper. Their settlement model was applied to consider the linear (long-term) evolution of ballast settlement. Further, Wang and Markine [11] concluded that the influence of differential settlement on track degradation is higher than the influence of stiffness variation in a transition between two track forms. Also, it was confirmed that the dynamic vehicle–track interaction is different when comparing transitions from soft to stiff or from stiff to soft track forms. Based on a model of the behaviour of granular material subjected to cyclic loading combined with a vehicle–track interaction model, Grossoni et al. [30] presented a semi-analytical approach that allows for the estimation of evolving track irregularities due to differential ballast settlement. Varandas et al. [21] presented a methodology to predict the settlement in a transition zone. Like the model to be presented in this paper, their methodology is based on simulations using a non-linear vehicle–track interaction model and an incremental settlement model. Zuada Coelho [31] predicted track settlement on a network scale by considering the effects of stochastic variations in traffic and soil conditions. A semi-analytical, frequency-domain cone model [32] based on the solution of a 1D wave propagation problem was applied to determine the dynamic stiffness and damping of the soil model. Examples of track models involving one-layer models, two-layer models with elastic/rigid sleepers, or three-layer models with sleepers and ballast masses used in simulations of dynamic vehicle–track interaction are reported in Refs. [33–36].

In this paper, a novel iterative procedure for the prediction of differential track settlement in a transition zone between ballasted track and slab track will be presented. The track model is a non-linear FE model accounting for gravity load, state-dependent foundation stiffness, and voided sleepers, while the empirical settlement equation is based on a visco–plastic material mechanics model approach. Non-linear load-deflection curves for the foundation/subgrade, rail pads and USPs can be considered. The dynamic vehicle–track interaction is solved using an extended state-space vector approach, and the redistribution of load in the track structure due to the evolving differential settlement is considered. To demonstrate the procedure, the influence of axle load in heavy haul traffic, and the implementation of USPs, on the long-term differential settlement in a transition between ballasted track and slab track will be investigated. The effect of various levels of initial misalignment in vertical rail level between the two track forms due to early consolidation and densification of ballast will also be studied.

2. The Swedish heavy haul line: traffic load and soil conditions

The Swedish heavy haul line Malmbanan is a single-track railway line in the northern part of Sweden. Traffic is dominated by iron ore freight trains with axle loads 30 t (tonnes) operating from the mines in Kiruna and Malmberget to the ports in Narvik (in Norway) and Luleå. The freight cars are supported and guided by three-piece bogies, and the speed of the loaded heavy haul trains is 60 km/h. The line is also used by passenger trains at maximum speed 135 km/h and by other freight trains with lower axle loads. The annual traffic load is of the order of 15 MGT (Mega Gross Tonnes) involving about 850,000 (loaded and unloaded) axle passages per year. The track design includes 60 kg/m rails, rail fastenings with 10 mm rubber rail pads, and concrete sleepers designed for an axle load of 35 t. The extreme weather conditions with temperatures down to −40 °C in the winter and relatively warm summers lead to recurrent issues with freeze-thaw conditions and evolving irregularities in track geometry due to differential settlement. The settlement rate along Malmbanan varies significantly depending on the local conditions and properties of the subgrade. Track geometry car recordings (longitudinal level) in the wavelength interval 1–25 m (D1) have been studied to provide information about typical levels of differential settlement [37]. For a selected 50 m section on Malmbanan, the degradation rate in terms of peak to mean value was of the order of 0.3 mm/year. This has been used as an indication of the order of typical differential settlement on Malmbanan in case of good track conditions [37,38].

In general, the resilient behaviour of ballast is highly governed by the kinematics and evolution of the inter-particle contact forces of the ballast when subjected to compressive and shear loading. On a particle-

particle level, when two particles are gradually pressed against each other, the contact surface increases and the rate of change of the contact stress decreases, leading to higher stiffness at higher level of applied pressure [39]. Furthermore, in these frictional materials the magnitude of the normal stress directly governs the magnitude of the shear stress that can be transferred (Coulomb friction). This partly explains the non-linear stress-strain path of ballast under compression load, where the aggregate stiffness is increasing with increasing stress levels. This was demonstrated in a field measurement on a track along the Swedish West Coast line (not Malmbanan) aiming to capture the relation between railseat load and sleeper displacement [40–42]. In that field test, an instrumented stationary railway wagon with two vertical servo-hydraulic cylinders was used to apply loads on the track. The ballast was a 300 mm thick layer of 32–64 mm granite macadam. The test was repeated by applying loads on several adjacent sleepers which had been unfastened from the rails. The sleeper with the applied load was instrumented with accelerometers, strain gauges, and a displacement gauge. At the test site, a stiff frame was constructed by driving four rods 2.5 to 4 m into the ground next to the track and connecting these by horizontal beams. This frame, shown in Fig. 1(a), was used as a rigid reference when the sleeper displacement was measured. The resulting static load-displacement characteristics measured for five adjacent sleepers are shown in Fig. 1(b). It is observed that the displacement of a sleeper end varies significantly from one sleeper to the next. For example, the spacing between sleepers S4 and S5 was only 0.65 m. Nevertheless, the displacement of the sleeper end to a static 50 kN force differed by a factor of two, which might be explained by that sleeper S4 was partially voided while sleeper S5 had better support conditions. Although the seated support stiffness seems to be relatively similar between the sleepers, it can be concluded that the ballast/subgrade stiffness may vary significantly from one sleeper to the next, and that the load-deflection curve for the ballast/sub-ballast is highly non-linear.

The most widely used model to describe the non-linear stress dependent stiffness of unbound granular materials (such as ballast) is the $K-\Theta$ model, or power law model, see [17,39],

$$E_r(p) = E_{ref}\left(\frac{p}{p_{ref}}\right)^{1-m} : p < 0 \quad (1)$$

Here, the resilience of the material is quantified by the modulus E_r, which is increasing considerably with increasing stress level p. Further, E_{ref} is the reference elasticity modulus determined at the reference stress p_{ref} (with a negative sign due to compression), and m is a calibration parameter. In this study, the reference stress is taken as $p_{ref} = -100$ kPa, while $m = 0.35$ [17,29].

As mentioned in Section 1, measurements of long-term differential settlement in a transition zone between ballasted track and 3 MB slab track on Malmbanan at a test site called Gransjö commenced in autumn 2022. An early report on these field measurements is available in reference [43]. To determine the properties of the layered substructure at this site, a Multi-Surface Analysis of Surface Waves (MASW) measurement has been performed. The MASW survey was designed to acquire Rayleigh wave data using vertical geophones (4.5 Hz natural frequency). The input signals were generated by striking an 8 kg sledgehammer vertically on an iron plate. The recording time was 1 s with a sampling interval of 250 μs. Along each section of aligned geophones, the measurements were performed at 2 m distance intervals, resulting in eight measurements along two sections each 14 m in length, and 13 measurements along one 24 m long section [44]. An example of the distribution of measured shear wave speed along one of the sections is shown in Fig. 2(a). The shear wave speed V_s is directly related to the small-strain shear modulus $G_0 = \rho V_s^2$, while Young's modulus is determined by $E = 2\rho\, V_s^2(1+\nu)$. Based on these measurements, four layers ($q = 4$) of the substructure (including the ballast and sub-ballast) with different properties have been identified, see Table 1. The stiffness properties from these geophysical tests are for small amplitudes of excitation, thus mostly reflect the integrated inter-particle stiffness at continuum scale without large particle re-arrangements. This reflects the state of a well compacted ballast layer.

Based on the data in Table 1, a 2D (plane strain) FE model of the layered soil has been developed in the commercial finite element software ABAQUS. The model includes four layers: ballast, sub-ballast and two layers of soil down to a depth of 12 m. The lower boundary of the fourth layer is rigid. Two versions of the model have been developed: (1) all four layers are linear elastic, (2) the ballast and sub-ballast layers are non-linear elastic based on the model in Eq. (1), while layers 3 and 4 are linear elastic. A hypo-elasticity material model is used to model the materials that exhibit non-linear, but reversible, stress and strain behaviour even at small strains. The two bottom layers are taken as linear elastic since it is assumed that the effect of the small stress amplitudes due to traffic loading has a negligible effect on their elastic performance. On the other hand, the two upper layers are subjected to higher stress amplitudes in the elastic or quasi-elastic regime, see [17,45].

To calculate the static load-deflection curve of the layered soil at the test site on Malmbanan, a 70 kN static load was applied on a rigid sleeper model placed on the ballast surface. The results for the two model versions (linear and non-linear) are shown in Fig. 2(b). Further, the

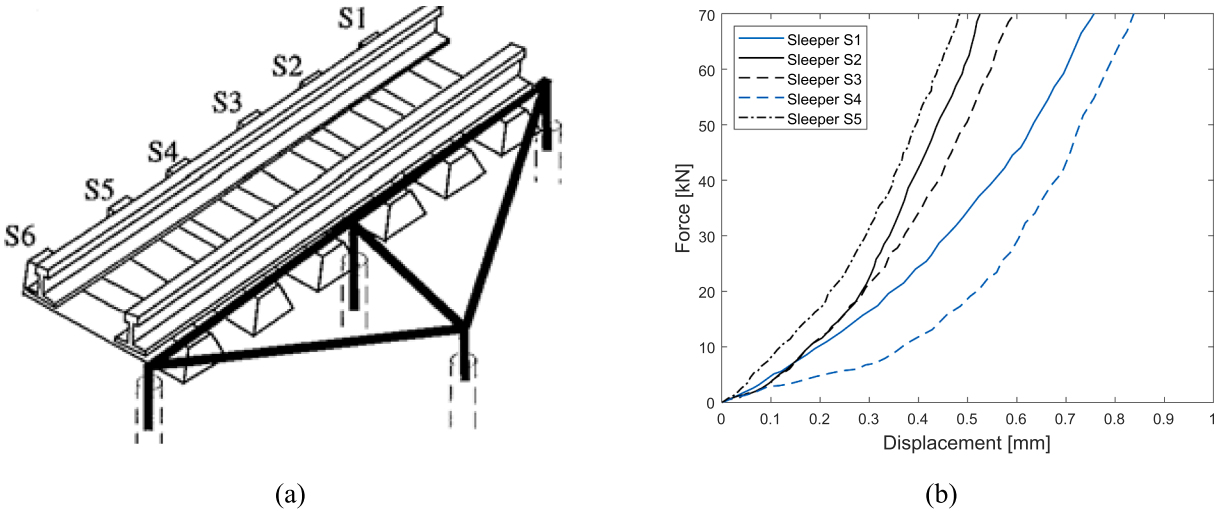

(a) (b)

Fig. 1. (a) Sketch of track and stiff frame used in the measurements on the Swedish West Coast line, and (b) applied static force versus measured sleeper end displacement for the case with unfastened rails and forces applied symmetrically on the two railseats of one sleeper. From [40].

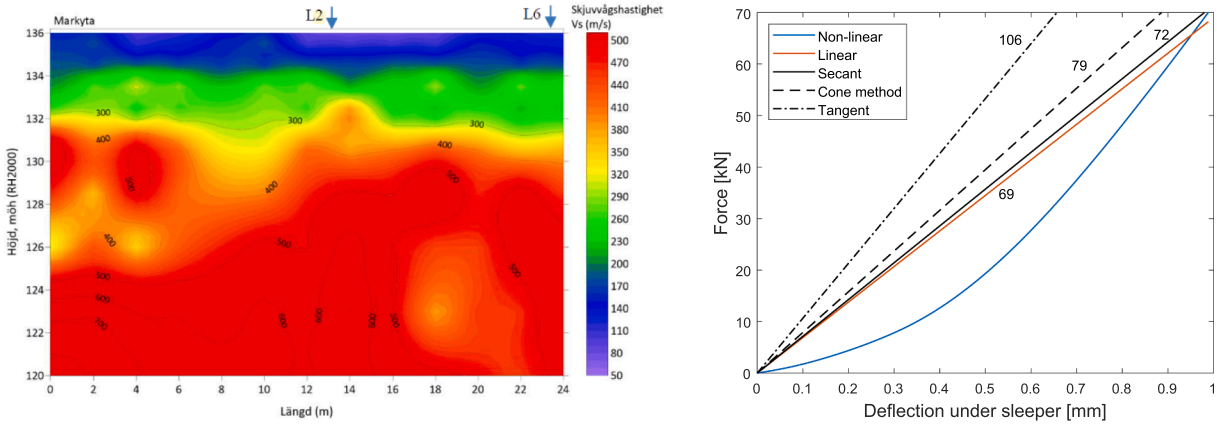

Fig. 2. Measured shear wave speed distribution of layered soil (from Ref. [44]), and (b) calculated force–displacement characteristic for foundation support stiffness at Gransjö. Linear(ised) stiffness values [kN/mm] per sleeper are indicated in the figure.

Table 1
Measured properties of the substructure layers at Gransjö. Based on data reported in [44] with layer number q, layer depth H, density ρ, Poisson's ratio ν, shear velocity V_s, reference elasticity modulus E_{ref} determined at reference stress $p_{ref} = -100$ kPa, resilience of material E, and minimum elasticity modulus E_{min}.

Layer	q	H (m)	ρ (kg/m^3)	ν (–)	V_s (m/s)	E (MPa)	E_{ref} (MPa)	m (–)	E_{min} (MPa)
Ballast (linear)	1	0.3	1800	0.2	125	67.5	–	–	–
Ballast (non-linear)	1	0.3	1800	0.2	125	–	115	0.35	15
Sub-ballast (linear)	2	1	2200	0.3	175	175	–	–	–
Sub-ballast (non-linear)	2	1	2200	0.3	175	–	175	0.35	30
Subgrade layer 1	3	2	1750	0.25	350	337	–	–	–
Subgrade layer 2	4	8	1750	0.25	>400	800	–	–	–

frequency-domain cone model [32] has been used to verify the FE model of the layered soil. The secant stiffness was determined as the ratio of maximum applied load to the corresponding maximum displacement. The tangent stiffness was calculated as the slope of a line tangent to the force-displacement curve at 0.9 mm deflection under sleeper. It is observed that the curve for the non-linear case has a high similarity with the measured curve in Fig. 1(b).

3. Simulation model

The simulation model is based on an iterative approach where a time-domain model of vertical dynamic vehicle–track interaction in the short term (accounting for voided sleepers and state-dependent properties of the ballast and subgrade at each sleeper–ballast interface) is integrated with an empirical model of accumulated ballast and subgrade settlement in the long term [22]. The simulation procedure is illustrated in Fig. 3. In each iteration step, one time-domain simulation of short-term vehicle–track dynamics is performed, where the pre-calculated static track displacement due to gravity load is used as initial conditions. The calculated load maxima at the interface between each sleeper and ballast in the ballasted track section, generated by the combination of gravity load and each of the passing wheels of the vehicle model, are identified and used as input to an empirical settlement model. In each iteration step, the track model is updated to account for the current states of the support conditions, and it is assumed that the same set of load maxima is generated by all passing vehicles. By taking several iteration steps, the accumulated differential settlement in the long term, the potential development of voided sleepers and the resulting

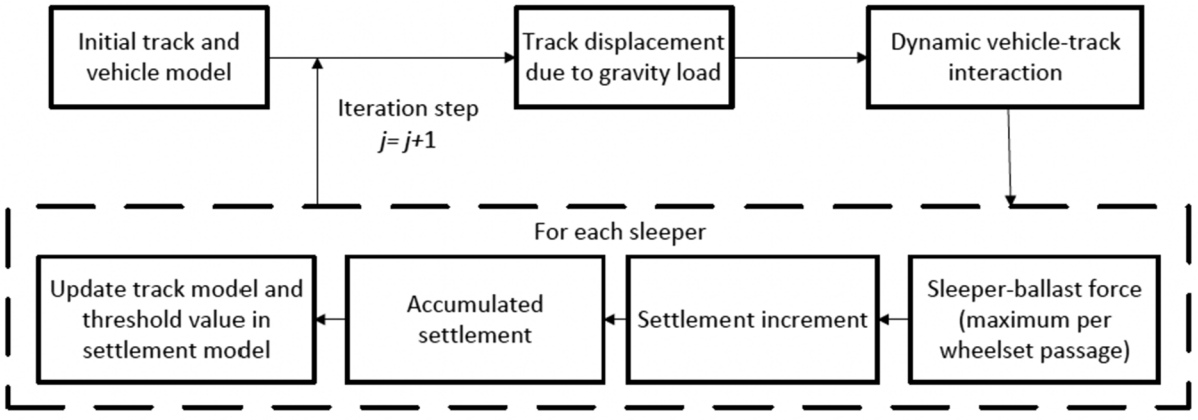

Fig. 3. Iterative procedure to predict differential settlement in a transition zone

redistribution of foundation loads between adjacent sleepers are calculated [8].

In this section, a 2D model for the simulation of vertical dynamic vehicle–track interaction in a transition zone between two different track forms is presented, see Fig. 4. The transition zone model consists of two track forms: a ballasted track and a 3 MB slab track [14]. The ballasted track model and the applied methodology to simulate the dynamic vehicle–track interaction have been verified in reference [46]. Based on the field measurements reported in [43], a calibration and verification of the full transition model will be carried out as the next step in this project. To reduce simulation time, symmetric vehicle and track properties with respect to a centre line between the two rails of the track are assumed. In addition, a symmetric excitation due to an initial misalignment in longitudinal level between the ballasted track and the slab track is prescribed. This means that only the wheels on one side of the wheelsets, one of the rails, half of the slab, and half sleepers are included in the model. In the demonstration examples in Section 4, the vehicle is moving from the ballasted track section to the slab track, but the opposite traffic direction could also be considered.

3.1. Vehicle model

The iron ore wagon used for heavy haul traffic on Malmbanan includes one car body and two three-piece bogies, each consisting of a bolster, two side frames and two wheelsets. The vehicle model in Fig. 4 has 14 degrees of freedom (DOFs), where two of the DOFs represent the motion (vertical displacement and pitch rotation) of the car body, four DOFs represent the corresponding displacements and rotations of the side frames (two DOFs per bogie), four DOFs the vertical displacement of the four wheelsets, while the four remaining massless DOFs (one per wheelset) are interfacing the rail and are used in the formulation of the constraint eqs. [36]. The unsprung mass of each wheelset is denoted M_w. Further, M_{bog} and J_{bog} are the mass and mass moment of inertia for each of the two side frames, while M_c and J_c are the mass and mass moment of inertia for the car body (including two bolsters). The axle distance within a bogie is Δ_w, while the bogie centre distance is Δ_{bog}. The vehicle model also includes the primary suspension stiffness k_1 and viscous damping c_1, and secondary suspension stiffness k_2 and viscous damping c_2. For traffic on tangent track, it is assumed that the car body and bolster are rigidly connected.

The sliding friction between bolster and side frame is modelled by a simplified Coulomb friction model using a hyperbolic tangent function [47]. This means that the force in the friction coupling is determined by

$$F = F_c \, tanh(\alpha \bullet v_{bs}) \tag{2}$$

where α is a factor that determines the rate of change of the tanh function (from -1 to $+1$), while v_{bs} is the relative sliding velocity between the bolster (here part of the car body) and side frame. The Coulomb sliding friction force is defined as $F_c = \mu N_c$, where μ is the coefficient of friction and N_c the normal load (car body load) in the sliding contact. This modelling approach can be seen as a computationally more efficient alternative to a conventional Coulomb friction model with the advantage that the force-velocity characteristic is smooth without any discontinuity in force between negative and positive sliding velocities.

The equations of motion for the vehicle are written in state-space form (with superscript v denoting vehicle) as

$$\begin{bmatrix} \mathbf{0} & \mathbf{0} & \mathbf{0} & \mathbf{0} \\ \mathbf{0} & \mathbf{0} & \mathbf{0} & \mathbf{M}^{v}_{bb} \\ \mathbf{I} & \mathbf{0} & \mathbf{0} & \mathbf{0} \\ \mathbf{0} & \mathbf{I} & \mathbf{0} & \mathbf{0} \end{bmatrix} \begin{Bmatrix} \dot{\mathbf{x}}^{v}_{a}(t) \\ \dot{\mathbf{x}}^{v}_{b}(t) \\ \ddot{\mathbf{x}}^{v}_{a}(t) \\ \ddot{\mathbf{x}}^{v}_{b}(t) \end{Bmatrix} + \begin{bmatrix} \mathbf{K}^{v}_{aa} & \mathbf{K}^{v}_{ab} & \mathbf{0} & \mathbf{0} \\ \mathbf{K}^{v}_{ba} & \mathbf{K}^{v}_{bb} & \mathbf{0} & \mathbf{C}^{v}_{bb} \\ \mathbf{0} & \mathbf{0} & -\mathbf{I} & \mathbf{0} \\ \mathbf{0} & \mathbf{0} & \mathbf{0} & -\mathbf{I} \end{bmatrix} \begin{Bmatrix} \mathbf{x}^{v}_{a}(t) \\ \mathbf{x}^{v}_{b}(t) \\ \dot{\mathbf{x}}^{v}_{a}(t) \\ \dot{\mathbf{x}}^{v}_{b}(t) \end{Bmatrix} + \begin{Bmatrix} \mathbf{Fa}(t) \\ \mathbf{0} \\ \mathbf{0} \end{Bmatrix} = \begin{Bmatrix} \mathbf{0} \\ \mathbf{F}^{ext}_{b} \\ \mathbf{0} \\ \mathbf{0} \end{Bmatrix} + \begin{Bmatrix} \mathbf{0} \\ \mathbf{F}^{\mu N}_{b}(t) \\ \mathbf{0} \\ \mathbf{0} \end{Bmatrix} \tag{3}$$

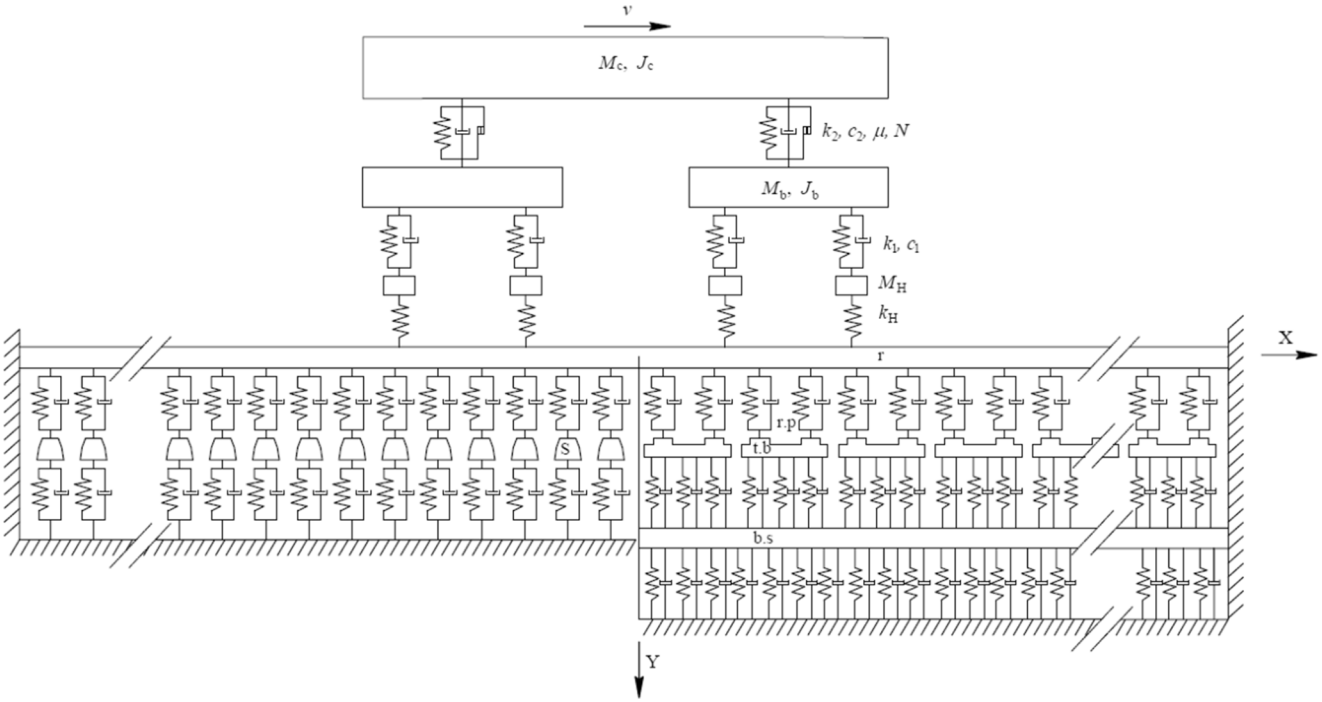

Fig. 4. Sketch of complete vehicle and transition zone model. The track model contains rail (r), top blocks (t.b) and base slab (b.s) modelled by beam elements. The base slab is supported by a Winkler foundation. The sleepers (s) are rigid masses supported by a spring-damper connection (representing the ballast/subgrade) with non-linear, and potentially random, stiffness properties.

In Eq. (3), the vertical displacements of the four massless DOFs of the vehicle interfacing the rail are collected in the 4 × 1 vector $\mathbf{x}_a^v(t)$, while $\mathbf{x}_b^v(t)$ is a 10 × 1 vector containing the non-interfacial vehicle degrees of freedom. The DOFs in $\mathbf{x}_b^v(t)$ represent the vertical displacements of the four (half) wheelsets of the leading and trailing bogies, the displacement and rotation of one side frame of each bogie, as well as the vertical displacement and rotation of the (half) car body. The contact forces between the wheels and rail are assembled in the 4 × 1 vector $\mathbf{F}a\,(t)$. Prescribed external loads (gravity load) are assembled in $\mathbf{F}_b^{ext}$, while $\mathbf{F}_b^{\mu N}(t)$ contains the friction forces between car body and side frames. Submatrices of the static stiffness matrix $\mathbf{K}^v$, the viscous damping matrix $\mathbf{C}^v$, and the mass matrix $\mathbf{M}^v$ of the vehicle are indicated in Eq. (3). The stiffness between each wheel (w) and the corresponding massless DOF is modelled using a non-linear Hertzian contact stiffness

$$k_{Hd,w} = C_H \left\langle x_{bd,w} - x_{ad,w} \right\rangle^{1/2}, d = \mathrm{l}, \mathrm{t}, w = 1, 2, \tag{4}$$

where C_H is the Hertzian constant, the Macaulay brackets are defined as $\langle \bullet \rangle = \frac{1}{2}(\bullet + |\bullet|)$. Subscripts l and t denote leading and trailing bogies, respectively. The matrices in Eq. (3) and the adopted parameter values for the vehicle model are given in Appendix A.

3.2. Track model

The non-linear track model, cf. Fig. 4, is a FE model with rigid boundaries at both rail ends and at the lower connection point of each spring/damper model representing the ballast and subgrade. The length of the track model is 60 m (corresponding to 42 m of ballasted track and 18 m of slab track). The 60E1 rail is modelled by Euler-Bernoulli beam theory with four beam elements in each sleeper bay. For this application, it has been confirmed that the selected track model length and the number of rail nodes per sleeper bay are sufficient to reach a condition at the transition where the effects of the boundaries and the discretisation are negligible. Each sleeper in the ballasted track section is modelled by a discrete (rigid) element with one vertical DOF and mass $m_s = 150$ kg. In this paper, the sleeper distance L = 0.6 m is taken as uniform, but this is not a constraint of the model. The sleepers and rail seats in the ballasted track are numbered with index i ($i = 1, 2, \ldots N_{bays}$-1: $i > 0$) starting from the transition, cf. Fig. 4. Further input data for the track model are summarised in Tables A.1 and A.2 in Appendix A.

The 3 MB concept is a reinforced standard precast slab design that strives to achieve fast and easy maintainability by the use of replaceable, precast components [14]. The rail is discretely supported at rail seat distance 0.6 m. The rail seats in the slab track are numbered with index i ($i = -1, -2, \ldots: i < 0$), cf. Fig. 4. The 3 MB track is based on 4.8 m long modules. Each module comprises a base slab, consisting of two longitudinal reinforced concrete beams that are connected by two transverse beams, and eight precast moulded concrete blocks, four on each longitudinal beam of the base slab. Elastomeric strips at the interfaces between base slab and blocks provide vibration attenuation and prevent the hammering of the moulded blocks against the base slab, see Fig. 5. In this paper, the base slab is modelled by one continuous beam, labelled by 'b.s', below the layer of discrete blocks, labelled by 't.b'. Both layers are modelled by Euler-Bernoulli beam theory. Each top block with two rail seats is represented by five beam elements, while the base slab has three beam elements per sleeper bay.

The foundation stiffness in the slab track section is modelled as linear and any evolution of settlement is neglected relative to the settlement in the ballasted track section [1]. This is because the contact pressure between base slab and foundation is expected to be significantly lower than the corresponding contact pressure at each sleeper. In each time step, the sleeper–ballast contact force at sleeper i is calculated as

$$F_{s/b,i} = \begin{cases} k_{b,i}\left(x_{s,i} - \Delta_i(n_s)\right) + c_{b,i}\dot{x}_{s,i} & \left(x_{s,i} - \Delta_i(n_s)\right) > 0 \\ 0 & \left(x_{s,i} - \Delta_i(n_s)\right) \le 0 \end{cases} \tag{5}$$

where the sleeper displacement $x_{s,i}$ is measured relative to the sleeper position before any load (gravity load and vehicle load) is applied on the track model and $\Delta_i(n_s)$ is the accumulated settlement for sleeper i in iteration step n_s. The accumulated settlement at each sleeper is evaluated relative to the virgin ballast surface level before any cyclic loading has been applied. Altogether this means that the sleeper–ballast force is zero until the corresponding calculated sleeper displacement exceeds the initial gap of a voided sleeper. Two alternative force–displacement characteristics for the support stiffness $k_{b,i}$ are illustrated in Fig. 6. It is assumed that the ratio $c_{b,i}/k_{b,i}$ is constant (here taken as 0.001, cf. [48]).

It is acknowledged that the selected track model, where ballast and subgrade is modelled by one-dimensional (non-linear) spring and damper elements, does not reflect the three-dimensional continuum of the foundation or the interaction between sleepers via the ground. An extension of the model by adding a discrete ballast mass below each sleeper and shear couplings between adjacent ballast masses, see [49], would be a simple approach to account for sleeper interaction via the ground at relatively low additional computational cost. It is suggested that the current version of the model is an attractive representation of a non-linear track that can be used for an optimisation of the superstructure in the transition zone. For example, it can be applied to optimise the (non-linear) stiffnesses of rail pads and USPs and/or the implementation of auxiliary rails. However, for a full optimisation of the transition zone design including its support conditions, an extended three-dimensional (continuum scale) model would be required but at a higher computational cost [16–20].

A potential initial misalignment in vertical level between the slab track and ballasted track, for example as a consequence of a densifica-

Fig. 5. A view of the 3 MB slab design consisting of base slabs, top blocks, and an elastomeric layer between the concrete layers.

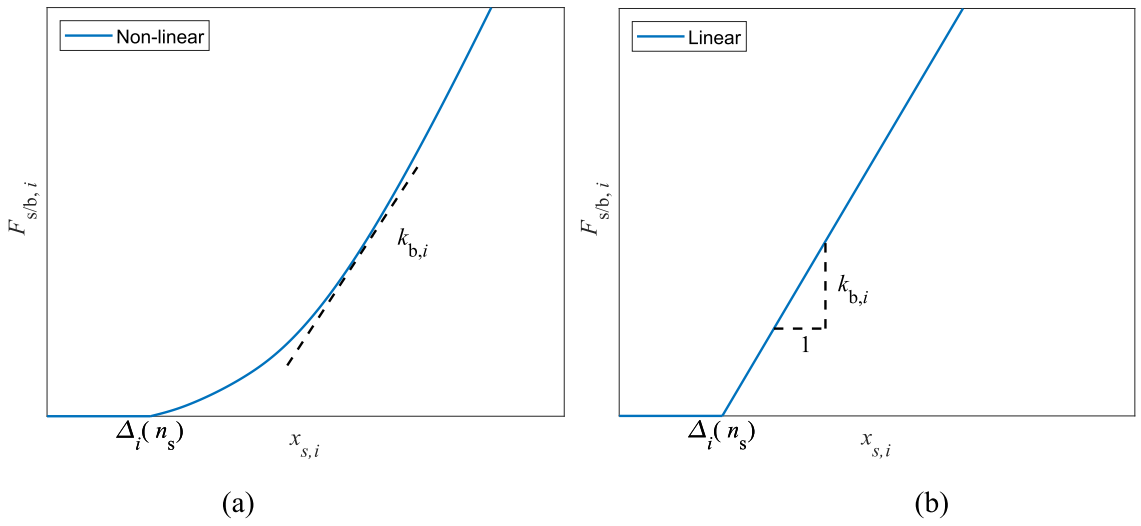

Fig. 6. Principle illustration of two alternative force–displacement characteristics for the spring modelling the foundation support stiffness (a) non-linear force–displacement, (b) piecewise linear force–displacement.

tion of the ballast layer after a few load cycles, can be accounted for by prescribing non-zero values for $\Delta_{i,j=1}$ for sleepers $i = 1, 2, \ldots N_{\text{bays}}$-1, cf. [2]. Such an initial misalignment would induce an additional dynamic loading of the vehicle–track system (due to a magnified pitching motion of the bogie) that would increase the settlement rate. In second-order form, the equations of motion for the track are written as

$$\begin{bmatrix} \mathbf{M}_{\text{ball}} & 0 & 0 \\ 0 & \mathbf{M}_{\text{coup}} & 0 \\ 0 & 0 & \mathbf{M}_{\text{slab}} \end{bmatrix} \begin{Bmatrix} \ddot{\mathbf{x}}^{\text{t}}_{\text{ball}}(t) \\ \ddot{\mathbf{x}}^{\text{t}}_{\text{coup}}(t) \\ \ddot{\mathbf{x}}^{\text{t}}_{\text{slab}}(t) \end{Bmatrix} + \begin{bmatrix} \mathbf{C}_{\text{ball}} & 0 & 0 \\ 0 & \mathbf{C}_{\text{coup}} & 0 \\ 0 & 0 & \mathbf{C}_{\text{slab}} \end{bmatrix} \begin{Bmatrix} \dot{\mathbf{x}}^{\text{t}}_{\text{ball}}(t) \\ \dot{\mathbf{x}}^{\text{t}}_{\text{coup}}(t) \\ \dot{\mathbf{x}}^{\text{t}}_{\text{slab}}(t) \end{Bmatrix} + \ldots$$

$$\begin{bmatrix} \mathbf{K}_{\text{ball}} & 0 & 0 \\ 0 & \mathbf{K}_{\text{coup}} & 0 \\ 0 & 0 & \mathbf{K}_{\text{slab}} \end{bmatrix} \begin{Bmatrix} \mathbf{x}^{\text{t}}_{\text{ball}}(t) \\ \mathbf{x}^{\text{t}}_{\text{coup}}(t) \\ \mathbf{x}^{\text{t}}_{\text{slab}}(t) \end{Bmatrix} = \mathbf{N}^{\text{T}}\mathbf{F}_{\text{a}}(t) + \mathbf{F}_{\text{s/b}}(t) + \mathbf{F}^{\text{t}}_{\text{g}}, \tag{6}$$

where $\mathbf{M}_{\text{ball}}$,$\mathbf{M}_{\text{coup}}$,$\mathbf{M}_{\text{slab}}$, $\mathbf{C}_{\text{ball}}$,$\mathbf{C}_{\text{coup}}$,$\mathbf{C}_{\text{slab}}$, $\mathbf{K}_{\text{ball}}$,$\mathbf{K}_{\text{coup}}$ and $\mathbf{K}_{\text{slab}}$ are the linear contributions to the mass, damping and stiffness matrices for the ballasted track, a short section of track including the interface between ballasted track and slab track, and the slab track, respectively. Thus, the DOFs of the track model can be assembled as $\mathbf{x}^{\text{t}} = \{\mathbf{x}^{\text{t,T}}_{\text{ball}}\ \mathbf{x}^{\text{t,T}}_{\text{coup}}\ \mathbf{x}^{\text{t,T}}_{\text{slab}}\}^{\text{T}}$. In Eq. (6), as in Eq. (3), $\mathbf{F}_{\text{a}}(\text{t})$ contains the time-variant wheel–rail contact forces. Further, the vector $\mathbf{F}_{\text{s/b}}$ contains the sleeper-ballast forces acting on each sleeper in the ballasted track section, while the constant vector $\mathbf{F}_{\text{g}}$ includes the gravity load on the superstructure. The equations of motion for the track can be rewritten in first-order form as

$$\begin{bmatrix} \mathbf{0} & \mathbf{M}^{\text{t}} \\ \mathbf{I} & \mathbf{0} \end{bmatrix} \begin{Bmatrix} \dot{\mathbf{x}}^{\text{t,T}}(\text{t}) \\ \dot{\mathbf{x}}^{\text{t,T}}(\text{t}) \end{Bmatrix} + \begin{bmatrix} \mathbf{K}^{\text{t}} & \mathbf{C}^{\text{t}} \\ \mathbf{0} & -\mathbf{I} \end{bmatrix} \begin{Bmatrix} \mathbf{x}^{\text{t,T}}(\text{t}) \\ \dot{\mathbf{x}}^{\text{t,T}}(\text{t}) \end{Bmatrix} - \begin{Bmatrix} \mathbf{N}^{\text{T}}\mathbf{F}\text{a}\ (t) \\ \mathbf{0} \end{Bmatrix} = \begin{Bmatrix} \mathbf{F}^{\text{t}}_{\text{s/b}}(\text{t}) + \mathbf{F}^{\text{t}}_{\text{g}} \\ \mathbf{0} \end{Bmatrix} \tag{7}$$

Note that each wheel–rail contact force in $\mathbf{F}\text{a}\ (t)$ is distributed as consistent forces and moments on the adjacent rail nodes using Hermitian interpolation polynomials contained in the block-diagonal matrix $\mathbf{N}$, see Section 3.3 and Ref. [36]. For the vehicle model with four wheel–rail contact points applied in the present paper, $\mathbf{N}$ is a 4 × 16 matrix.

3.3. Constraint equations

In each time step, the position of the vehicle along the track model is determined, and each wheel–rail contact force is distributed on the two adjacent rail nodes based on the Hermitian interpolation polynomials [50–52]

$$N_1 = 1 - \frac{3\xi^2}{L^2} + \frac{2\xi^3}{L^3}\ N_2 = -\xi + \frac{2\xi^2}{L} - \frac{\xi^3}{L^2} \tag{8a}$$

$$N_3 = \frac{3\xi^2}{L^2} - \frac{2\xi^3}{L^3}\ N_4 = \frac{\xi^2}{L} - \frac{\xi^3}{L^2} \tag{8b}$$

The interpolation polynomials are assembled in the matrix $\mathbf{N}$ with ξ being a local length co-ordinate for each beam element. The constraints on the interfacial displacements, velocities, and accelerations for the massless DOFs $\mathbf{x}^{\text{v}}_{\text{a}}$ of the vehicle upon assuming a prescribed vehicle speed $v(t)$, and considering the Coriolis and centripetal accelerations that occur because the vehicle model is moving along the track model, are formulated as

$$\mathbf{x}^{\text{v}}_{\text{a}}(t) = \mathbf{N}\mathbf{x}^{\text{t}}_{\text{int}}(t) + \mathbf{x}^{\text{irr}} \tag{9a}$$

$$\dot{\mathbf{x}}^{\text{v}}_{\text{a}}(t) = \mathbf{N}\dot{\mathbf{x}}^{\text{t}}_{\text{int}}(t) + \frac{\mathbf{dN}}{\mathbf{d}\xi}v\mathbf{x}^{\text{t}}_{\text{int}}(\text{t}) + \dot{\mathbf{x}}^{\text{irr}} \tag{9b}$$

$$\ddot{\mathbf{x}}^{\text{v}}_{\text{a}}(\text{t}) = \mathbf{N}\ddot{\mathbf{x}}^{\text{t}}_{\text{int}}(t) + \frac{\mathbf{d}^2\mathbf{N}}{\mathbf{d}^2\xi}v^2\mathbf{x}^{\text{t}}_{\text{int}}(t) + 2\frac{\mathbf{dN}}{\mathbf{d}\xi}v\dot{\mathbf{x}}^{\text{t}}_{\text{int}}(t) + \frac{\mathbf{dN}}{\mathbf{d}\xi}\dot{v}\mathbf{x}^{\text{t}}_{\text{int}}(t) + \ddot{\mathbf{x}}^{\text{irr}} \tag{9c}$$

with $\dot{\mathbf{x}}^{\text{irr}}$ and $\ddot{\mathbf{x}}^{\text{irr}}$ defined as

$$\dot{\mathbf{x}}^{\text{irr}} = \frac{\mathbf{dx}^{\text{irr}}}{\mathbf{d}\xi}v \text{ and } \dot{\mathbf{x}}^{\text{irr}} = \frac{\mathbf{d}^2\mathbf{x}^{\text{irr}}}{\mathbf{d}\xi^2}v^2 + \frac{\mathbf{d}\dot{\mathbf{x}}^{\text{irr}}}{\mathbf{d}\xi}\dot{v} \tag{10}$$

The first term on the right-hand side of Eq. (9c) can be recognised as the acceleration of the track. Eqs. (9b) and (9c) can be rewritten as, cf. [36],

$$\dot{\mathbf{x}}^{\text{v}}_{\text{a}}(t) = \mathbf{T}(t)\dot{\mathbf{x}}^{\text{t}}_{\text{int}}(t) + \mathbf{U}(t)\mathbf{x}^{\text{t}}_{\text{int}}(t) + \dot{\mathbf{x}}^{\text{irr}} \tag{11a}$$

$$\ddot{\mathbf{x}}^{\text{v}}_{\text{a}}(t) = \mathbf{T}(t)\ddot{\mathbf{x}}^{\text{t}}_{\text{int}}(t) + \mathbf{R}(t)\dot{\mathbf{x}}^{\text{t}}_{\text{int}}(t) + \mathbf{S}(t)\mathbf{x}^{\text{t}}_{\text{int}}(t) + \ddot{\mathbf{x}}^{\text{irr}} \tag{11b}$$

where

$$\mathbf{T}(t) = \mathbf{N}, \mathbf{U}(t) = \frac{\mathbf{dN}}{\mathbf{d}\xi}v \tag{11c}$$

$$\mathbf{R}(t) = 2\frac{\mathbf{dN}}{\mathbf{d}\xi}v, \mathbf{S}(t) = \frac{\mathbf{d}^2\mathbf{N}}{\mathbf{d}\xi^2}v^2 + \frac{\mathbf{dN}}{\mathbf{d}\xi}\dot{v} \tag{11d}$$

Here $\boldsymbol{x}^{\mathrm{irr}}$ contains the prescribed wheel/rail surface irregularities (neglected in the present paper), while $\mathbf{x}^{\mathrm{t}}_{\mathrm{int}}$ contains the four rail DOFs that are adjacent to each wheel–rail contact.

3.4. Initial conditions of vehicle and track displacements

To reduce the time for each simulation of dynamic vehicle–track interaction, the vehicle is set to start from a position between the left rail boundary and the transition, but where the vehicle is not yet significantly influencing the dynamic response of the transition. For the track model, the initial displacement vector $\mathbf{x}^{\mathrm{t}}_{\mathrm{init}}(t=0) = \{\mathbf{x}^{\mathrm{t,T}}_{\mathrm{ball,\ init}}\ \mathbf{x}^{\mathrm{t,T}}_{\mathrm{coup,\ init}}\ \mathbf{x}^{\mathrm{t,T}}_{\mathrm{slab,\ init}}\}$ due to the gravity loads of vehicle and track is calculated by solving the non-linear matrix equation

$$\begin{bmatrix} \mathbf{K}_{\mathrm{ball}} & 0 & 0 \\ 0 & \mathbf{K}_{\mathrm{coup}} & 0 \\ 0 & 0 & \mathbf{K}_{\mathrm{slab}} \end{bmatrix} \mathbf{x}^{\mathrm{t}}_{\mathrm{init}} - \mathbf{F}_{\mathrm{stat}}\left(\mathbf{x}^{\mathrm{t}}_{\mathrm{init}}\right) = \mathbf{0}, \tag{12a}$$

$$\mathbf{F}_{\mathrm{stat}}\left(\mathbf{x}^{\mathrm{t}}_{\mathrm{init}}\right) = \mathbf{N}^{\mathrm{T}}\mathbf{F}_{\mathrm{a}}(t=0) + \mathbf{F}_{\mathrm{g}} + \mathbf{F}_{\mathrm{s/b}}\left(\mathbf{x}^{\mathrm{t}}_{\mathrm{init}}\right) \tag{12b}$$

Here each element in $\mathbf{F}_{\mathrm{a}}(t=0)$ corresponds to the static wheel load (half of the axle load). Eq. (12a) is solved in Matlab using the solver *fsolve* (with the trust-region dogleg algorithm). As in Eqs. (12a) and (12b), $\mathbf{K}_{\mathrm{ball}}$,$\mathbf{K}_{\mathrm{coup}}$, and $\mathbf{K}_{\mathrm{slab}}$ are the linear stiffness matrices for the ballasted, coupled, and slab sections of track excluding the state-dependent stiffness of the ballast/subgrade below each sleeper in the ballasted track section.

3.5. Simulation of vertical dynamic vehicle–track interaction

For a case where the track model can be taken as linear and a complex-valued modal superposition can be applied to reduce computational cost, the methodology for the simulation of vertical dynamic vehicle–track interaction is described in detail in Nielsen and Igeland [36]. In this study, where the track model is non-linear, the simulation is instead performed by a direct integration in the time domain. However, note that a methodology for the simulation of differential settlement in ballasted track, using a complex-valued modal superposition approach for the linear partition of a state-dependent track model, was presented in [22].

An extended (mixed) state–space vector $\boldsymbol{z}(t)$ is introduced as.

$$z(t) = \left\{ \mathbf{x}^{\mathrm{t,T}}\ \dot{\mathbf{x}}^{\mathrm{t,T}}\ \mathbf{x}^{\mathrm{v,T}}_{\mathrm{a}}\ \mathbf{x}^{\mathrm{v,T}}_{\mathrm{b}}\ \dot{\mathbf{x}}^{\mathrm{v,T}}_{\mathrm{a}}\ \dot{\mathbf{x}}^{\mathrm{v,T}}_{\mathrm{b}}\ \widehat{\mathbf{F}}^{\mathrm{T}}_{\mathrm{a}}(t) \right\} \tag{13}$$

It includes the displacements $\mathbf{x}^{\mathrm{t}}$ and velocities $\dot{\mathbf{x}}^{\mathrm{t}}$ of the transition zone track model and the displacements $\mathbf{x}^{\mathrm{v}}$ and velocities $\dot{\mathbf{x}}^{\mathrm{v}}$ of the vehicle model. Further, it contains the impulses $\widehat{\mathbf{F}}_{\mathrm{a}}(t) = \int \mathbf{F}_{\mathrm{w/r}}(t)\,\mathrm{d}t$ of the wheel–rail contact forces. This allows for that all equations of motion for vehicle and track, and the constraint equations coupling the vehicle and track, can be assembled in one first-order matrix form as

$$\mathbf{A}(z,t)\dot{z} + \mathbf{B}(z,t)z = \mathbf{F}(z,t) \tag{14}$$

with

$$\mathbf{A}(z,t) = \begin{bmatrix} \mathbf{0} & \mathbf{M}^{\mathrm{t}} & \mathbf{0} & \mathbf{0} & \mathbf{0} & \mathbf{0} & -\mathbf{N}^{\mathrm{T}} \\ \mathbf{I} & \mathbf{0} & \mathbf{0} & \mathbf{0} & \mathbf{0} & \mathbf{0} & \mathbf{0} \\ \mathbf{0} & \mathbf{I} & \mathbf{0} & \mathbf{0} & \mathbf{0} & \mathbf{0} & \mathbf{I} \\ \mathbf{0} & \mathbf{0} & \mathbf{0} & \mathbf{0} & \mathbf{0} & \mathbf{M}^{\mathrm{v}}_{\mathrm{bb}} & \mathbf{0} \\ \mathbf{0} & \mathbf{0} & \mathbf{0} & \mathbf{I} & \mathbf{0} & \mathbf{0} & \mathbf{0} \\ \mathbf{T} & \mathbf{0} & \mathbf{0} & \mathbf{0} & -\mathbf{I} & \mathbf{0} & \mathbf{0} \\ \mathbf{R} & \mathbf{T} & -\mathbf{I} & \mathbf{0} & \mathbf{0} & \mathbf{0} & \mathbf{0} \end{bmatrix} \tag{15a}$$

$$\mathbf{B}(z,t) = \begin{bmatrix} \mathbf{K}^{\mathrm{t}} & \mathbf{C}^{\mathrm{t}} & \mathbf{0} & \mathbf{0} & \mathbf{0} & \mathbf{0} & \mathbf{0} \\ \mathbf{0} & -\mathbf{I} & \mathbf{0} & \mathbf{0} & \mathbf{0} & \mathbf{0} & \mathbf{0} \\ \mathbf{0} & \mathbf{0} & \mathbf{K}^{\mathrm{v}}_{\mathrm{aa}} & \mathbf{K}^{\mathrm{v}}_{\mathrm{ab}} & \mathbf{0} & \mathbf{0} & \mathbf{I} \\ \mathbf{0} & \mathbf{0} & \mathbf{K}^{\mathrm{v}}_{\mathrm{ba}} & \mathbf{K}^{\mathrm{v}}_{\mathrm{bb}} & \mathbf{0} & \mathbf{C}^{\mathrm{v}}_{\mathrm{bb}} & \mathbf{0} \\ \mathbf{0} & \mathbf{0} & \mathbf{0} & \mathbf{0} & \mathbf{0} & -\mathbf{I} & \mathbf{0} \\ \mathbf{U} & \mathbf{0} & \mathbf{0} & \mathbf{0} & \mathbf{0} & \mathbf{0} & \mathbf{0} \\ \mathbf{S} & \mathbf{0} & \mathbf{0} & \mathbf{0} & \mathbf{0} & \mathbf{0} & \mathbf{0} \end{bmatrix} \tag{15b}$$

Eq. (14) contains the governing equations of motion for the track, Eq. (7), for the vehicle, Eq. (3), and the algebraic constraint equations, Eqs. (9b) and (9c). The mixed force vector $\mathbf{F}$ is written as

$$\mathbf{F}(z,t) = \left\{ \mathbf{F}^{\mathrm{t,T}}_{\mathrm{s/b}}(t) + \mathbf{F}^{\mathrm{t,T}}_{\mathrm{g}}\ \mathbf{0}^{\mathrm{T}}\ \mathbf{0}^{\mathrm{T}}\ \mathbf{F}^{\mathrm{v},ext,\mathrm{T}}_{\mathrm{b}}(t)\ \mathbf{0}^{\mathrm{T}}\ \dot{\mathbf{x}}^{\mathrm{irr}}\ \ddot{\mathbf{x}}^{\mathrm{irr}} \right\}^{\mathrm{T}} \tag{16}$$

The initial value problem for the solution of the transient vibration problem is then obtained as

$$\dot{z} = \mathbf{A}^{-1}(\mathbf{F} - \mathbf{B}z), z(t=0) = z_0 \tag{17}$$

where $\boldsymbol{z}_0$ includes the initial state from Section 3.4. In the present study, the solution is obtained by using MATLAB's moderately stiff differential equation solver ode23s.

3.6. Settlement model

The aim of the iterative procedure, see Fig. 3, is to calculate the long-term accumulated differential settlement and track geometry degradation for a given traffic load corresponding to a given number of load cycles (wheel passages). In each iteration step, after solving the short-term vehicle–track interaction problem in the time domain, the time history of each sleeper–ballast force is calculated in a post-processing step using the FE model of the track. For each vehicle model passage in iteration step j ($j = 1, 2, \ldots n_{\mathrm{s}}$), the incremental settlement $\delta_{i,j}$ [m] at sleeper i ($i = 1, 2, \ldots N_{\mathrm{bays}}$-1) is formulated as a function of the maxima of the sleeper–ballast contact force $F_{\mathrm{s/b},i}$

$$\delta_{i,j} = \sum_{n=1}^{N_{\mathrm{w}}} \left\{ \sum_{k=1}^{N_k} \alpha_k \left[\frac{\left\langle max\left(F_{\mathrm{s/b},i}\right)_n - F_{\mathrm{th},i} \right\rangle}{F_0} \right]^{\beta_k} \right\} \tag{18}$$

where N_{w} is the number of wheels in the vehicle model (here, $N_{\mathrm{w}} = 4$). Within each iteration step, it is assumed that the set of max ($F_{\mathrm{s/b},i}$) remains the same for all vehicle passes such that a linear extrapolation of the settlement increment to represent up to 10^5 load cycles can be carried out, see below. The order N_k of the polynomial formulation and the corresponding parameters α_k and β_k are empirical, while $F_0 = 1$ kN is a reference contact force with a unit such that the term within the square brackets becomes non-dimensional. The settlement model used here is similar to the one suggested by Sato [53] in the sense that there is no accumulation of permanent ballast/subgrade deformation if the maximum sleeper–ballast contact force generated by a passing wheel is below a certain threshold value $F_{\mathrm{th},i}$. This is reflected in Eq. (18) by the Macaulay brackets. Furthermore, it is assumed that the model provides the permanent deformation accounting for all the layers of the substructure.

The accumulated settlement at sleeper i after n_{s} iteration steps (corresponding to N_{s} wheel passings) is calculated by summing the incremental settlements calculated for each preceding step j as

$$\Delta_i(n_s) = \sum_{j=1}^{n_s} \delta_{i,j} \tag{19}$$

In the next iteration step, these accumulated settlements are applied in the updated track model. For each sleeper i, it is assumed that the

current threshold value $F_{th,i}$ is dependent on the accumulated settlement Δ_i as:

$$F_{th,i}(\Delta_i) = F_{th,\infty} - \left(F_{th,\infty} - F_{th,0}\right) e^{-\gamma \Delta_i} \tag{20}$$

where $F_{th,\,0}$ is the virgin threshold value before any traffic loading has been applied, $F_{th,\,\infty}$ is the long-term threshold value corresponding to a completely stabilised (consolidated) track, while γ is a parameter that determines the rate of hardening. The parameters of the threshold value are track site specific. Thus, in future work, these parameters (as well as α_k and β_k) need to be calibrated against field measurements. As inspired by a visco-plastic material mechanics formulation, the threshold value is dependent on the accumulated settlement. This leads to a non-linear hardening (increase) of the threshold value with increasing settlement, see Fig. 7, and consequently to a decreasing settlement rate with increasing accumulated traffic load.

In each iteration step, up to 10^5 load cycles (corresponding to 3 MGT of traffic with loaded iron ore trains) are considered. However, an adaptive step length is applied such that the maximum allowed settlement increment δ^{max} per iteration step is limited. If the increment exceeds δ^{max}, a linear interpolation is applied. A convergence study on the influence of the settlement increment per iteration step on the accumulated settlement was presented in [22], and it was concluded that $\delta^{max} = 0.2$ mm provides a reasonable compromise between accuracy and computational cost.

The number of load cycles $N_{s,j}$ in iteration step j is determined by the maximum settlement increment appearing at any of the sleepers in the model. Thus, if $\max(\delta_{i,\,j}) > \delta^{max}$, all calculated $\delta_{i,\,j}$ are scaled linearly such that

$$\delta_{i,j} = \frac{\delta^{max}}{max\left(\delta_{i,j}\right)} \delta_{i,j} \tag{21}$$

The number of load cycles accounted for in iteration step j is

$$N_{s,j} = \frac{\delta^{max}}{max\left(\delta_{i,j}\right)} \bullet 10^5, \tag{22}$$

where $N_{s,j}$ is converted to the nearest integer. However, if $\max(\delta_{i,\,j}) \leq \delta^{max}$, then the $\delta_{i,\,j}$ calculated by Eq. (18) are maintained and $N_{s,j} = 10^5$. This procedure is used to limit the change of characteristics for the state-dependent ballast/subgrade models between two consecutive iteration steps.

4. Demonstration of model

To demonstrate the iterative model presented in Section 3, a parameter study has been carried out to investigate the influence of the different input parameters of the empirical model on the predicted sleeper settlement. Further, the effects of increasing the axle load and implementing USPs in the transition zone on the dynamic vehicle–track interaction and sleeper settlement will be studied. Piecewise linear and non-linear models of the sleeper support (ballast and subgrade) will be compared. One-way traffic of loaded iron ore trains at speed 60 km/h in the direction from stiffer track to softer track is assumed.

A random variation of support stiffness can be prescribed along the track model. However, in this study, it is assumed that the bed modulus [(N/m)/m^2] of the virgin foundation is uniform along and across the track on both sides of the transition. Since the base area of the sleepers is smaller than for the base slab, the stiffness of the foundation is lower on the ballasted side. On the other hand, the rail pad stiffness is lower on the slab track side. Altogether, the static track stiffness at rail level is higher on the ballasted side leading to a gradient in track stiffness that contributes to the dynamic (transient) excitation of the vehicle–track system, see Fig. 8.

Based on the tangent stiffness evaluated for the non-linear soil model, see Section 2 and Fig. 2(b), the linearised support stiffness per half sleeper is taken as $k_{bi} = 100$ kN/mm ($i = 1, 2, \ldots N_{bays}$-1). Since the base area of half a sleeper is 0.34 m^2, this corresponds to a bed modulus k_f in the order of 300 MN/m^3, see Table A.2 in Appendix A. It is assumed that the same bed modulus can be applied on both sides of the transition. Thus, the Winkler bed stiffness for the base slab $k_s = 168$ (kN/mm)/m. In combination with the different stiffnesses at each rail seat for the two track forms, this leads to a gradient in stiffness at rail level occurring at the transition, see Fig. 8. The selected value for the piecewise linear stiffness of the sleeper support is used in the simulations referred to as 'linear', see below. For the 'non-linear' simulations, the non-linear force–displacement curve illustrated in Fig. 2(b) has been applied for all sleepers.

As an example, the calculated displacement for Sleeper 5 in iteration 1 is shown in Fig. 9(a). The corresponding sleeper–ballast contact force is illustrated in Fig. 9(b). It is observed that the sleeper displacement from the non-linear model is significantly larger than from the linear model due to the lower support stiffness at low loads, while the maximum sleeper–ballast contact force from the non-linear model is slightly higher than from the linear model. For both sleeper support

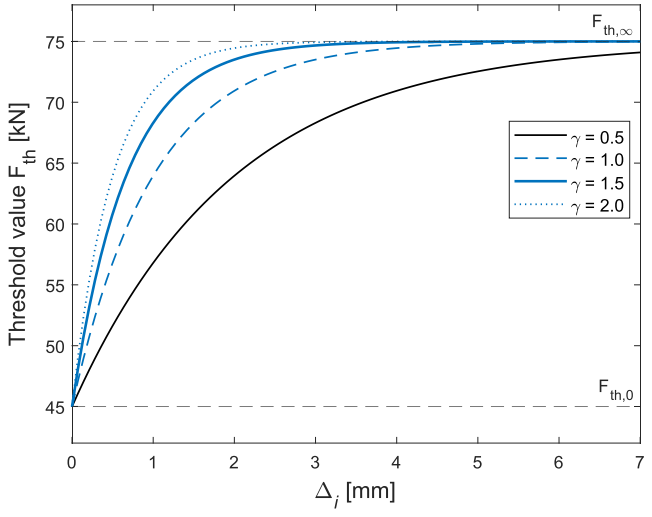

Fig. 7. Influence of hardening parameter γ and accumulated settlement Δ_i on threshold value F_{th} (here: $F_{th,0} = 45$ kN and $F_{th,\,\infty} = 75$ kN).

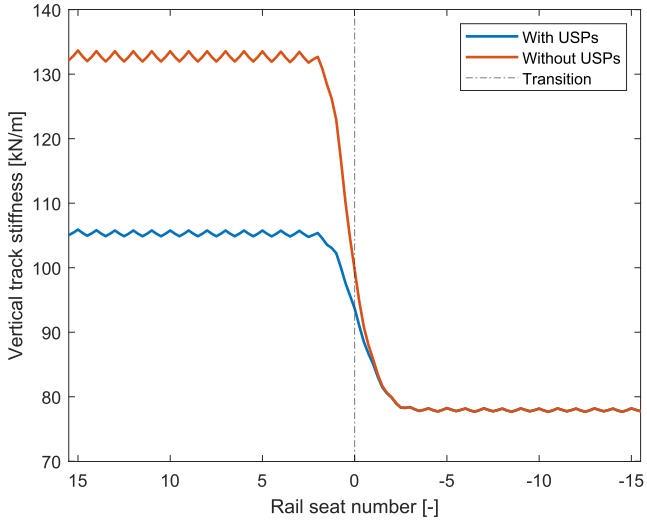

Fig. 8. Static track stiffness at rail level along the transition with or without USPs on the ballasted side. The vertical line indicates the position of the transition. Rail seat numbers are positive on the ballasted side.

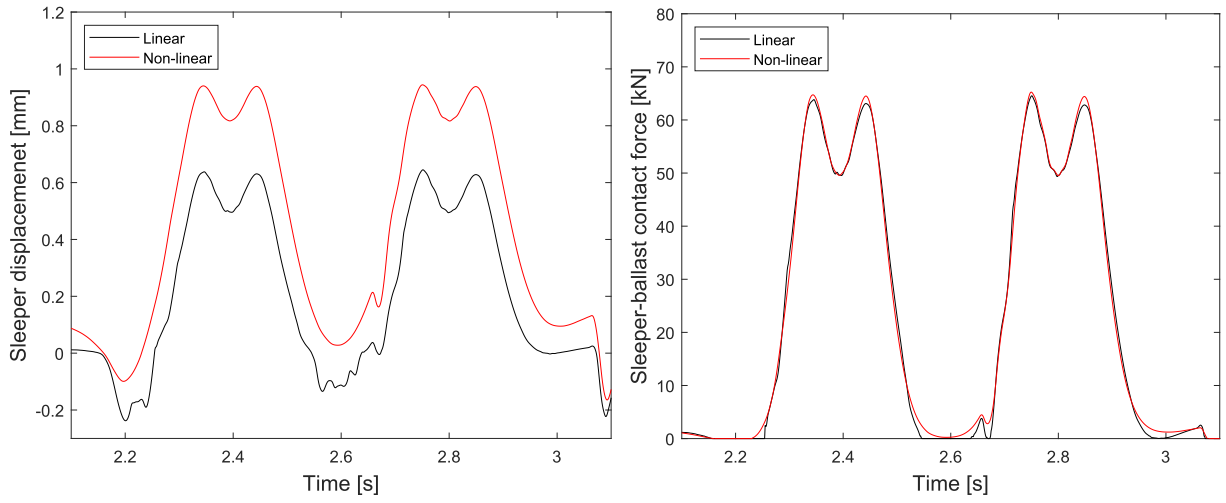

Fig. 9. Calculated (a) sleeper displacement and (b) sleeper–ballast contact force evaluated for piecewise linear and non-linear models of the sleeper support stiffness. Results are presented for Sleeper 5 from the transition, first iteration

stiffness models, the sleeper–ballast force drops to zero when there is loss of contact between sleeper and ballast.

4.1. Parameterization of empirical settlement model

When applying Eqs. (18)–(20) to predict the accumulated settlement under each sleeper, the following input parameters are required: $F_{\text{th, 0}}$, $F_{\text{th, }\infty}$, γ, N_k, α_k and β_k. In this paper, it is assumed that a first-order form of Eq. (18) is sufficient. Thus, $N_k = 1$ and $\beta_1 = 1$. The influence of the remaining parameters $F_{\text{th, 0}}$, $F_{\text{th, }\infty}$, γ and α_1 on the simulated accumulated settlement after three years of traffic is studied next. To tune the input parameters, the uniform settlement rate of the ballasted track model at sufficient distance from the transition is compared to the differential settlement rate measured for well-supported track sections on Malmbanan. Track geometry degradation on a 10 km section of track between Kaisepakte and Stordalen (km 1484–1494) on the northern branch of Malmbanan was evaluated in [38]. Based on recurrent track geometry car measurements between 1997 and 2016, a representative degradation rate in terms of peak to mean value for a track support in good condition can be expected to be in the order of 0.3 mm/year.

For an accumulated traffic load of 45 MGT (three years of traffic with loaded iron ore trains), the influences of $F_{\text{th, 0}}$, $F_{\text{th, }\infty}$, γ and α_1 on the accumulated settlement per sleeper along the transition zone are quantified and illustrated in Fig. 9. The applied reference input to the model was $F_{\text{th, 0}} = 45$ kN, $F_{\text{th, }\infty} = 75$ kN, $\gamma = 0.5$, and $\alpha_1 = 1$ mm per 10^5 load cycles. Then, one parameter was varied at a time while the other parameters remained at their reference values. An initial vertical rail misalignment was assumed by prescribing $\Delta_{\text{init}} = 2$ mm uniform settlement for all sleepers on the ballasted side in the first iteration. Note that the stiffness gradient and the initial rail misalignment leads to a pitching motion of the two bogies and the car body resulting in a transient dynamic loading of the track and higher sleeper–ballast forces adjacent to the transition [54]. This leads to larger accumulated settlements for the sleepers adjacent to the transition, which can be observed as a local maximum in settlement near the transition in all figures.

In Figs. 10(a,b), it can be seen that the accumulated settlement per sleeper is increasing with decreasing γ and $F_{\text{th, 0}}$. For lower values of γ, the change in accumulated settlement is significant as the threshold value remains relatively low also for larger accumulated settlements. Further, in Figs. 10(c,d), it is observed that the accumulated settlement is increasing with increasing values of α_1 and decreasing values of $F_{\text{th, }\infty}$. It can be argued that lower values for the initial and infinite thresholds correspond to a track support that is more susceptible to settlement. By comparing the accumulated sleeper settlement far from the transition (as measured from the initial state) after three years of traffic with the measured reference settlement rate from Malmbanan, see above, reasonable input data to the settlement model can be determined. Based on this initial parameter study, it is observed that the reference input data listed above leads to a predicted accumulated settlement in the order of 1.2 mm, which is in qualitative agreement with the measured settlement rate. Thus, the applied settlement model with the reference setup has been verified and will be used in the following simulations. Further, an adaptive step length (number of load cycles) has been applied such that the maximum allowed settlement increment $\delta^{\max} = 0.2$ mm, see Section 3.6 and Ref. [22]. A further calibration of these input data will be carried out based on the long-term field test on Malmbanan that commenced in autumn 2022, see Section 1 and [43].

The influence of different prescribed initial levels Δ_{init} for all sleepers in the ballasted track section on the accumulated sleeper settlement after three years of traffic load is illustrated in Fig. 11(a). It can be concluded that a large initial misalignment at the transition, for example due to early consolidation and densification of the ballast or an error in the initial levelling of the track, will lead to a substantial dynamic loading of the system and a larger dip in rail level adjacent to the transition.

To illustrate a result from the iterative calculation procedure up to an accumulated traffic load of 45 MGT, the calculated accumulated sleeper settlement after each iteration step is shown in Fig. 11(b). For the considered vehicle load and the given parameters in the applied settlement model, a continuous accumulation of settlement below all sleepers in the ballasted track is observed. However, as discussed above, due to the stiffness variation and the misalignment in rail level there is a dynamic excitation of the vehicle–track system leading to more settlement (local maximum) at the sleepers adjacent to the transition. This will create a loop of increasing dynamic excitation of the system leading to higher sleeper–ballast contact forces, further settlement, etc. Note that the development of voided sleepers near the transition leads to a redistribution of load to the adjacent sleepers (towards higher sleeper numbers). This will generate higher settlement at these adjacent sleepers, and a small shift in the location of the local maximum away from the transition. However, due to the increase (hardening) of the settlement threshold value with increasing accumulated settlement, there is eventually a stabilisation (slowing down) of the settlement.

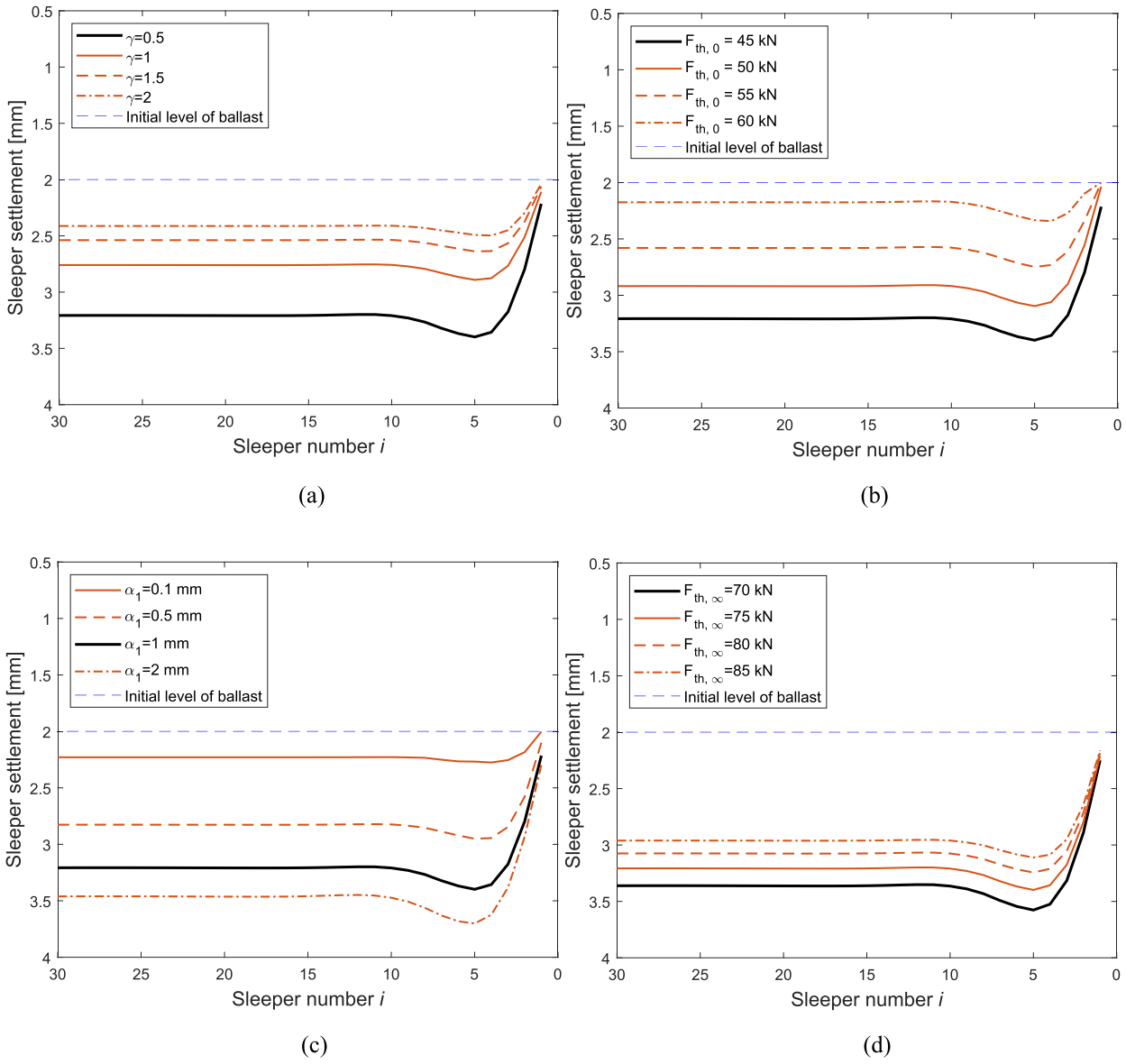

Fig. 10. Influence of input parameters on accumulated sleeper settlement Δ after three years of traffic (45 MGT): (a) hardening parameter γ, (b) initial threshold value $F_{\text{th, 0}}$, (c) scaling parameter α_1, (d) infinite threshold value $F_{\text{th, }\infty}$. Initial rail misalignment due to initial level of ballast $\Delta_{\text{init}} = 2$ mm. Sleepers are numbered from the transition. Slab foundation stiffness 168 (kN/mm)/m, support stiffness per half sleeper 100 kN/mm.

4.2. Axle load and implementation of USPs

To evaluate the influences of stiffness gradient and initial misalignment, the dynamic responses of the transition zone with or without initial misalignment on the ballasted side will be compared. Thus, in the model of the transition zone without initial misalignment, only the stiffness gradient between the ballasted track and slab track has been considered. The influence of axle load on the calculated time history of the vertical wheel–rail contact force at the transition is illustrated in Fig. 12(a). It can be concluded that the stiffness gradient at the transition leads to a minor contribution to the dynamic load, while the influence of the irregularity is more significant. The corresponding calculated rail displacement due to gravity load (no vehicle load, cf. Section 3.4) due to the accumulated sleeper settlement after a traffic load of 45 MGT is shown in Fig. 12(b). For the same initial misalignment, it is observed that an increase of axle load leads to a considerable increase of settlement, both in terms of a higher uniform settlement away from the transition and a larger local maximum (dip). The influence of stiffness gradient and axle load is further studied in [54].

Next, the influence of implementation of USPs in the transition zone is investigated. USPs in transition zones are used as a specific measure in track superstructure design to smoothen and reduce the gradient in track stiffness at rail level. Based on input from Getzner [55], the dynamic bedding modulus of the applied USP has been selected as 0.42 N/mm^3. Considering a sleeper base area of 0.68 m^2 [56], this results in a discrete spring stiffness of 142 kN/mm per half sleeper to represent the stiffness of the USP that is coupled in series with the already considered support stiffness k_{bi} of the ballast and subgrade. The influence of implementing USPs on the maximum sleeper–ballast contact force at the transition after one iteration is illustrated in Fig. 13(a). As expected, it can be observed that the USPs lead to lower sleeper–ballast contact forces due to a better load distribution along the track model. When considering all cases illustrated in Fig. 13(a), sleeper–ballast contact forces are generally higher for Sleepers 3–7 than elsewhere, and the maximum sleeper–ballast contact force exceeds the initial threshold value for all sleepers except Sleeper 1.

The maximum sleeper–ballast contact force evaluated over all sleepers along the transition in each iteration step is shown in Fig. 13(b).

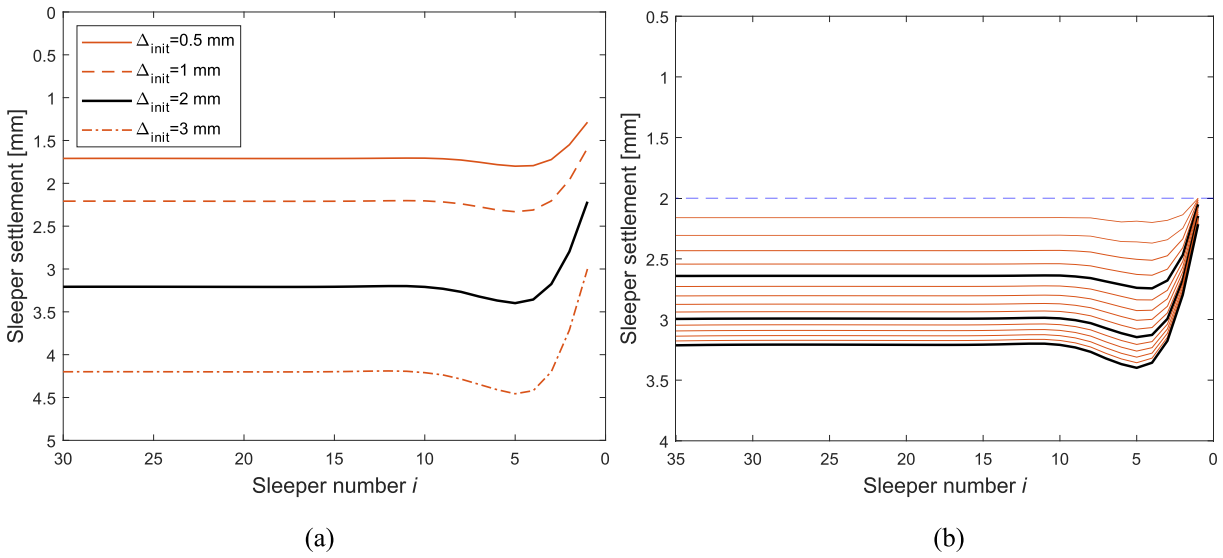

Fig. 11. Accumulated sleeper settlement Δ after three years of traffic (45 MGT). (a) Influence of initial level Δ_{init}, (b) illustration of results from iterative procedure (15 iterations of sleeper settlement, $\Delta_{init} = 2$ mm, settlement after 1, 2 and 3 years are indicated by black solid lines). Slab foundation stiffness 168 (kN/mm)/m, support stiffness per half sleeper 100 kN/mm.

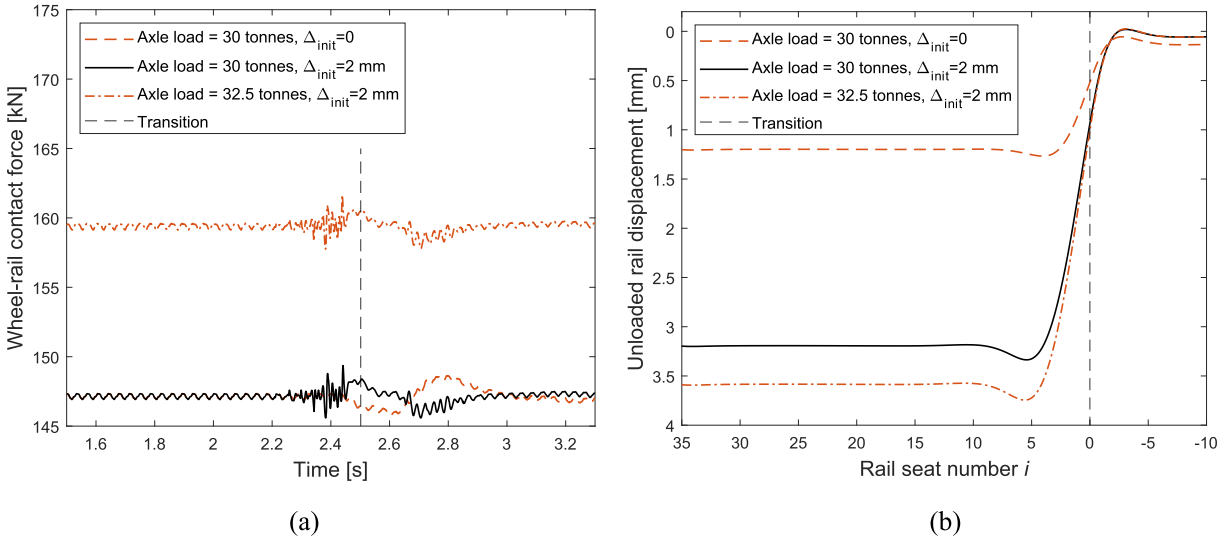

Fig. 12. Influence of axle load and initial misalignment on (a) time history of wheel–rail contact force along the transition (results from the first iteration of the simulation procedure), (b) rail displacement due to gravity load after an accumulated traffic load of 45 MGT.

It is observed that the maximum sleeper–ballast contact force for the non-linear model without USPs (axle load 30 t) is higher than for the corresponding linear model without USPs because the secant stiffness of the non-linear model is lower than the linearised stiffness 100 kN/mm, leading to a better distribution of load along the track model. Further, it can be seen that the maximum sleeper–ballast contact force in the early iteration steps is higher than in later iterations. In combination with the lower threshold value for smaller accumulated settlement, this leads to a higher sleeper settlement rate in the early iteration steps, see Fig. 13(c). The use of USP reduces the track stiffness at rail level and leads to a wider distribution of load along the sleepers and along the track. Thus, by implementing USPs, the maximum sleeper–ballast contact forces are reduced, see Fig. 13(b), as well as settlement rate and accumulated settlement, see Figs. 13(c,d). Note that the influence of USP may vary depending on the specific USP parameters and track configuration, see Refs. [49,50]. For example, in this study an improvement can be found at higher axle load compared to the results without USP due to more uniform contact pressure, see Fig. 13(d). As a result, to determine the benefit of USP, a further investigation including predictions of long–term ballast settlement and dynamic behaviour is required.

5. Conclusions

An iterative procedure to predict the long-term degradation of longitudinal level in a transition zone between ballasted track and slab track due to differential accumulated settlement of ballasted track has been presented. Gravity loads and state-dependent track conditions are accounted for, including situations involving a prescribed (and random) variation of sleeper support stiffness along the track model. Non-linear load-deflection curves for the foundation/subgrade, rail pads and USPs can be considered. An empirical settlement model based on a visco–plastic material mechanics model approach has been presented, and the influence of its input parameters on the predicted settlement has been investigated. The applied settlement model is similar to the one

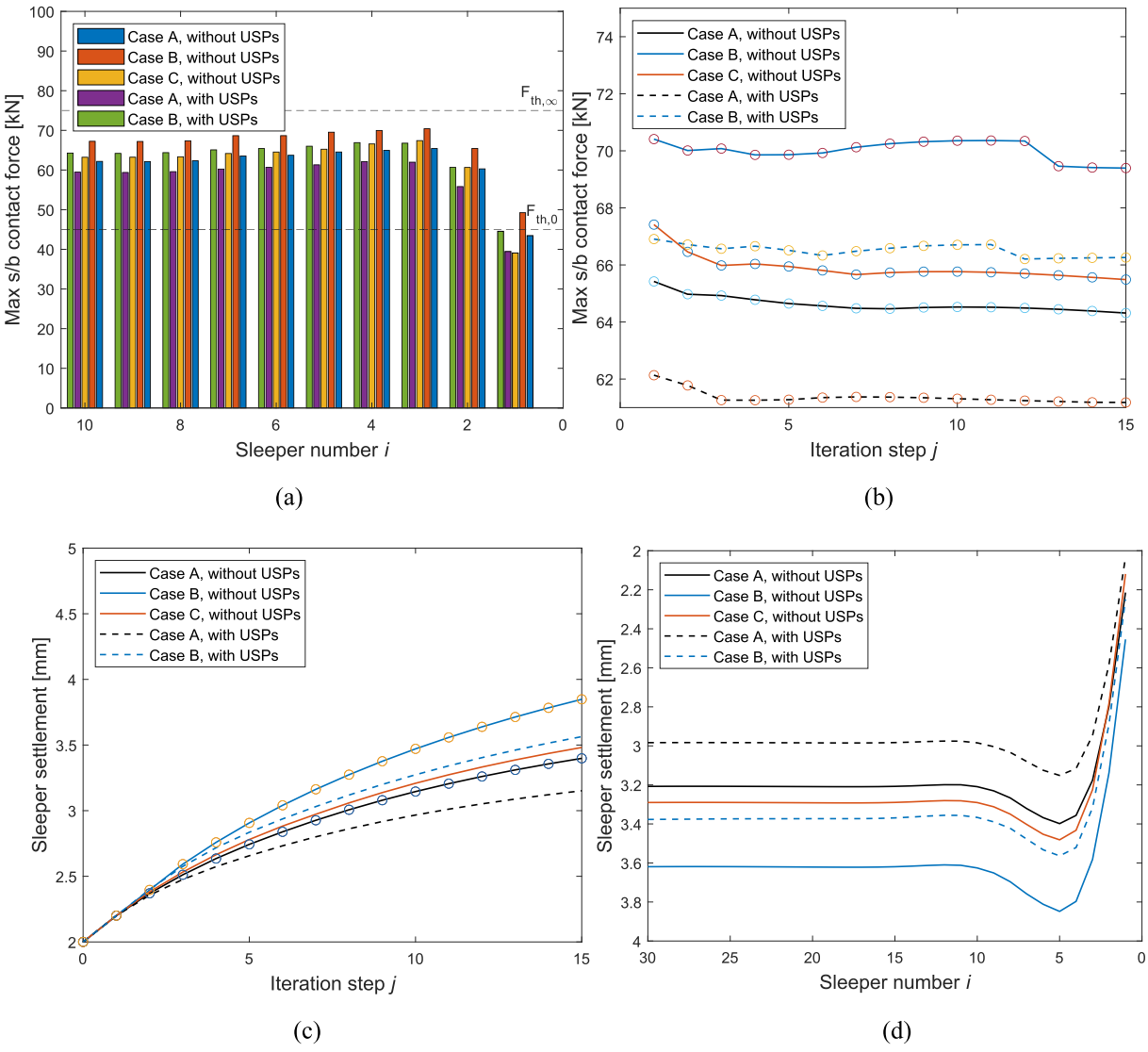

Fig. 13. The influence of implementing USPs on sleeper settlement after three years of traffic (45 MGT, $\Delta_{\text{init}} = 2$ mm). Case A: linear model of the sleeper support stiffness and axle load 30 t; Case B: linear model of the sleeper support stiffness and axle load 32.5 t; Case C: non-linear model of the sleeper support stiffness and axle load 30 t. (a) Maximum sleeper–ballast contact force along the transition zone in the first iteration, (b) maximum sleeper–ballast contact force per iteration evaluated over all sleepers, (c) maximum accumulated sleeper settlement per iteration evaluated over all sleepers, (d) accumulated settlement per sleeper along the transition zone after 45 MGT.

suggested by Sato [53] in the sense that an increment in settlement only takes place if the sleeper-ballast contact load exceeds a threshold value. However, the threshold value is dependent on the accumulated settlement. This leads to a non-linear hardening (increase) of the threshold value with increasing settlement, and consequently to a decreasing settlement rate with increasing accumulated traffic load. The level of simulated uniform settlement away from the transition has been verified against measured data from the field. The procedure has been demonstrated for heavy haul traffic by simulating the long-term degradation of longitudinal level as initiated by a prescribed misalignment on the ballasted track side, as well as the influence of increased axle load and the implementation of USPs.

It has been shown that the distribution of forces transmitted to the ballast varies considerably along a transition zone. This is due to the stiffness gradient at the transition, but even more so should there be an initial misalignment in rail level at the transition for example due to a densification of ballast after the first few load cycles. In both cases, a transient pitching motion of the passing vehicles is generated leading to a contribution to the dynamic loading. This results in higher levels of settlement at sleepers near the transition than elsewhere because the sleeper–ballast contact forces are higher and exceed the prescribed threshold value in the settlement model. The linearisation of the sleeper support stiffness model, representing the properties of the track substructure, leads to an underestimation of the accumulated settlement of the ballast.

As expected, the uniform settlement ahead of the transition and the vertical track irregularity (local maximum in rail displacement due to gravity load) at the transition were found to increase with increasing axle load. It was shown that the consideration of a non-linear hypoelastic model for the ballast and sub-ballast is a viable and adequate option for the constitutive representation of the ballast and sub-ballast in these long-term simulations. Nevertheless, the alternative of a linear(ised) model is convenient from the point of view of computational effort.

Author statement

None.

Declaration of Competing Interest

None.

Data availability

Data will be made available on request.

Acknowledgments

The current study is part of the ongoing activities in CHARMEC – Chalmers Railway Mechanics (www.chalmers.se/charmec). Parts of the study have been funded from the European Union's Horizon 2020 research and innovation programme in the projects In2Track2 and In2Track3 under grant agreements Nos 826255 and 101012456. Discussions with Dr. Saeed Hossein Nia, Mr. Ingemar Persson and Mr. Carlos Hermosilla are gratefully acknowledged. Parts of the simulations were performed using resources at Chalmers Centre for Componential Science and Engineering (C3SE) provided by the Swedish National Infrastructures for Computing (SNIC).

Appendix A. Input data for track and vehicle models

The input data to the Euler-Bernoulli beam elements and discrete spring and damper elements used in the track model are presented in Tables A.1 and A.2. Each layer of beam elements has bending stiffness $EI_{A,}$[1] mass m_A per unit beam length, width b_A and height h_A that may vary along the longitudinal track coordinate. Subscripts 'r', 't.b', and 'b.s' denote rail, top block, and base slab, respectively. In Table A.2, the subscript 'f' denotes foundation, while 'r/s', 'r/t.b', and 't.b,b.s' denote the coupling between rail-sleeper and rail-top block and top block-base slab, respectively.

The input data for the vehicle model collected from Refs. [1,57] are listed in Table A.3. However, the model of sliding friction between car body and side frame has been modified. The vehicle model was validated against a more extensive and three-dimensional model in the commercial software GENSYS. The masses M_c, M_{bog}, and M_w denote the mass of the car body, bogie, and wheelset, whereas J_c and J_{bog} denote the pitch inertia of the car body and bogie. Further the stiffness and viscus damping of the primary and secondary suspensions are denoted k_1, k_2, c_1, and c_2, whereas Δ_w denotes the longitudinal wheelset spacing in a bogie, and Δ_{bog} denotes the longitudinal distance between the two bogie centra.

Table A.1
Beam properties in the track model.

Rail	$EI_r = 6.4$ MNm^2	$m_r = 60$ kg/m		
Top block	$EI_{t.b} = 11$ MNm^2	$m_{t.b} = 275$ kg/m	$b_{t.b} = 0.55$ m	$h_{t.b} = 0.2$ m
Base slab	$EI_{b.s} = 23.45$ MNm^2	$m_{b.s} = 375$ kg/m	$b_{b.s} = 0.6$ m	$h_{b.s} = 0.25$ m

Table A.2
Stiffness and damping of resilient layers in the track model. Note that k_f and c_f are stiffness and damping per unit area, respectively.

Stiffness	$k_f = 300$ MN/m^3	$k_{r/s} = 120$ MN/m	$k_{r/t.b} = 40$ MN/m	$k_{t.b/b.s} = 1.0$ GN/m^3
Damping	$c_f = 246$ kNs/m^3	$c_{r/s} = 25$ kNs/m	$c_{r/t.b} = 10$ kNs/m	$c_{t.b/b.s} = 250$ kNs/m

Table A.3
Parameter values for vehicle model with axle load 30 t.

$M_c = 111\times 10^3$ kg	$J_c = 1.7\times 10^6$ kgm^2	$k_1 = 30$ MN/m	$c_1 = 70$ kNs/m	$\Delta_{bog} = 6.77$ m
$M_{bog} = 800$ kg	$J_{bog} = 730$ kgm^2	$k_2 = 3.75$ MN/m	$c_2 = 10$ kNs/m	$\Delta_w = 1.78$ m
$M_w = 1341$ kg	$J_w = 100$ kgm^2	$\alpha = 5$	$\mu = 0.25$	$N_c = 550\times 10^3$ N

For the vehicle model, the mass, damping, and stiffness matrices specified in Eq. (3) are given below. The four interfacial DOFs (between wheel and rail) are indicated by subscript a. The 10 non-interfacial DOFs are indicated by subscript b, where DOF numbers 1–4 correspond to DOFs of the leading bogie, DOF numbers 5–8 of the trailing bogie, and DOF numbers 9–10 of the car body.

$$\mathbf{M}_{bl,bl} = \mathbf{M}_{bt,bt} = \frac{\mathbf{1}}{\mathbf{2}}\begin{bmatrix} M_w & 0 & 0 & 0 \\ 0 & M_w & 0 & 0 \\ 0 & 0 & M_{bog} & 0 \\ 0 & 0 & 0 & J_{bog} \end{bmatrix}, \tag{A.1a}$$

$$\mathbf{M}_{c,c} = \frac{\mathbf{1}}{\mathbf{2}}\begin{bmatrix} M_c & 0 \\ 0 & J_c \end{bmatrix}, \tag{A.1b}$$

$$\mathbf{M}_{bb}^{v} = \begin{bmatrix} \mathbf{M}_{bl,bl} & \mathbf{0} & \mathbf{0} \\ \mathbf{0} & \mathbf{M}_{bt,bt} & \mathbf{0} \\ \mathbf{0} & \mathbf{0} & \mathbf{M}_{c,c} \end{bmatrix}, \tag{A.1c}$$

[1] Replace B with k or c depending on if it is a spring or a damper.

$$\mathbf{C}_{\mathrm{bl,bl}} = \mathbf{C}_{\mathrm{bt,bt}} = \begin{bmatrix} c_1 & 0 & -c_1 & -c_1\Delta_{\mathrm{w}}/2 \\ 0 & c_1 & -c_1 & c_1\Delta_{\mathrm{w}}/2 \\ -c_1 & -c_1 & 2c_1+c_2 & 0 \\ -c_1\Delta_{\mathrm{w}}/2 & c_1\Delta_{\mathrm{w}}/2 & 0 & c_1\Delta_{\mathrm{w}}^2/2 \end{bmatrix}, \tag{A.2a}$$

$$\mathbf{C}_{\mathrm{c,bl}} = \mathbf{C}_{\mathrm{bl,c}}^{\mathrm{T}} = \begin{bmatrix} 0 & 0 & -c_2 & 0 \\ 0 & 0 & -c_2\Delta_b/2 & 0 \end{bmatrix}, \tag{A.2b}$$

$$\mathbf{C}_{\mathrm{c,bt}} = \mathbf{C}_{\mathrm{bt,c}}^{\mathrm{T}} = \begin{bmatrix} 0 & 0 & c_2 & 0 \\ 0 & 0 & c_2\Delta_b/2 & 0 \end{bmatrix}, \tag{A.2c}$$

$$\mathbf{C}_{\mathrm{c,c}} = \begin{bmatrix} 2c_2 & 0 \\ 0 & c_2\Delta_b^2/2 \end{bmatrix}, \tag{A.2d}$$

$$\mathbf{C}_{\mathrm{bb}}^{\mathrm{v}} = \begin{bmatrix} \mathbf{C}_{\mathrm{bl,bl}} & \mathbf{0} & \mathbf{C}_{\mathrm{bl,c}}^{\mathrm{T}} \\ \mathbf{0} & \mathbf{C}_{\mathrm{bt,bt}} & \mathbf{C}_{\mathrm{bt,c}}^{\mathrm{T}} \\ \mathbf{C}_{\mathrm{c,bl}} & \mathbf{C}_{\mathrm{c,bt}} & \mathbf{C}_{\mathrm{c,c}} \end{bmatrix}, \tag{A.2e}$$

$$\mathbf{K}_{\mathrm{aa}}^{\mathrm{v}} = \begin{bmatrix} k_{\mathrm{Hl},1} & 0 & 0 & 0 \\ 0 & k_{\mathrm{Hl},2} & 0 & 0 \\ 0 & 0 & k_{\mathrm{Ht},1} & 0 \\ 0 & 0 & 0 & k_{\mathrm{Ht},1} \end{bmatrix}, \tag{A.3a}$$

$$\mathbf{K}_{\mathrm{a,bl}} = \mathbf{K}_{\mathrm{bl,a}}^{\mathrm{T}} = \begin{bmatrix} -k_{\mathrm{Hl},1} & 0 & 0 & 0 \\ 0 & -k_{\mathrm{Hl},2} & 0 & 0 \\ 0 & 0 & 0 & 0 \\ 0 & 0 & 0 & 0 \end{bmatrix}, \tag{A.3b}$$

$$\mathbf{K}_{\mathrm{a,bt}} = \mathbf{K}_{\mathrm{bt,a}}^{\mathrm{T}} = \begin{bmatrix} 0 & 0 & 0 & 0 \\ 0 & 0 & 0 & 0 \\ -k_{\mathrm{Ht},1} & 0 & 0 & 0 \\ 0 & -k_{\mathrm{Ht},2} & 0 & 0 \end{bmatrix}, \tag{A.3c}$$

$$\mathbf{K}_{\mathrm{bi,bi}} = \begin{bmatrix} k_1+k_{\mathrm{Hi},1} & 0 & -k_1 & -k_1\Delta_w/2 \\ 0 & k_1+k_{\mathrm{Hi},2} & -k_1 & k_1\Delta_w/2 \\ -k_1 & -k_1 & 2k_1+k_2 & 0 \\ -k_1\Delta_w/2 & k_1\Delta_{\mathrm{w}}/2 & 0 & k_1\Delta_w^2/2 \end{bmatrix}, i = l,t, \tag{A.3d}$$

$$\mathbf{K}_{\mathrm{c,bl}} = \mathbf{K}_{\mathrm{bl,c}}^{\mathrm{T}} = \begin{bmatrix} 0 & 0 & -k_2 & 0 \\ 0 & 0 & -k_2\Delta_b/2 & 0 \end{bmatrix} \tag{A.3e}$$

$$\mathbf{K}_{\mathrm{c,bt}} = \mathbf{K}_{\mathrm{bt,c}}^{\mathrm{T}} = \begin{bmatrix} 0 & 0 & k_2 & 0 \\ 0 & 0 & k_2\Delta_b/2 & 0 \end{bmatrix}, \tag{A.3f}$$

$$\mathbf{K}_{\mathrm{c,c}} = \begin{bmatrix} 2k_2 & 0 \\ 0 & k_2\Delta_{\mathrm{b}}^2/2 \end{bmatrix}, \tag{A.3g}$$

$$\mathbf{K}_{\mathrm{bb}}^{\mathrm{v}} = \begin{bmatrix} \mathbf{K}_{\mathrm{bl,bl}} & \mathbf{0} & \mathbf{K}_{\mathrm{bl,c}} \\ \mathbf{0} & \mathbf{K}_{\mathrm{bt,bt}} & \mathbf{K}_{\mathrm{bt,c}} \\ \mathbf{K}_{\mathrm{c,bl}} & \mathbf{K}_{\mathrm{c,bt}} & \mathbf{K}_{\mathrm{c,c}} \end{bmatrix}, \tag{A.3h}$$

$$\mathbf{K}_{\mathrm{ab}}^{\mathrm{v}} = \mathbf{K}_{\mathrm{ba}}^{\mathrm{v,T}} = \begin{bmatrix} \mathbf{K}_{\mathrm{a,bl}} & \mathbf{K}_{\mathrm{a,bt}} & \mathbf{0} \end{bmatrix}, \tag{A.3i}$$

References

[1] Aggestam E, Nielsen JCO. Multi-objective optimisation of transition zones between slab track and ballasted track using a genetic algorithm. J Sound Vib 2019;446:91–112.

[2] Wang H, Markine V. Modelling of the long-term behaviour of transition zones: prediction of track settlement. Eng Struct 2018;156:294–304.

[3] Paixão A, Varandas JN, Fortunato E. Dynamic behavior in transition zones and long-term railway track performance. Front Built Environ 2021;7:1–16.

[4] Ognibene G, Powrie W, Le Pen L, Harkness J. Analysis of a bridge approach: Long-term behaviour from short-term response. In: 15th Int Conf Railw Eng; 2019.

[5] Paixão A. Transition zones in railway tracks: An experimental and numerical study on the structural behaviour (Ph.D. thesis). Porto, Portugal: The Faculty of Engineering of University of Porto; 2014.

[6] Sañudo R, Dell'Olio L, Casado JA, Carrascal IA, Diego S. Track transitions in railways: a review. Construct Build Mater 2016;112:140–57.

[7] Coelho B, Hölscher P, Priest J, Powrie W, Barends F. An assessment of transition zone performance. Proc Inst Mech Eng F: J Rail Rapid Transit 2011;225:129–39.

[8] Varandas JN, Paixão A, Fortunato E. A study on the dynamic train-track interaction over cut-fill transitions on buried culverts. Comput Struct 2017;189:49–61.

[9] Paixão A, Varandas JN, Fortunato E, Calçada R. Numerical simulations to improve the use of under sleeper pads at transition zones to railway bridges. Eng Struct 2018;164:169–82.
[10] Indraratna B, Babar Sajjad M, Ngo T, Gomes Correia A, Kelly R. Improved performance of ballasted tracks at transition zones: a review of experimental and modelling approaches. Transp Geotech 2019;21:100260.
[11] Wang H, Markine V. Dynamic behaviour of the track in transitions zones considering the differential settlement. J Sound Vib 2019;459:114863.
[12] Aggestam E, Nielsen JCO, Bolmsvik R. Simulation of vertical dynamic vehicle–track interaction using a two-dimensional slab track model. Veh Syst Dyn 2018;56:1633–57.
[13] Aggestam E, Nielsen JCO, Lundgren K, Zandi K, Ekberg A. Optimisation of slab track design considering dynamic train–track interaction and environmental impact. Eng Struct 2022;254:113749.
[14] Morales-Gamiz FJ. Design requirements, concepts, and prototype test results for new system of ballastless system (3MB slab track). 2017.
[15] Chumyen P, Connolly DP, Woodward PK, Markine V. The effect of soil improvement and auxiliary rails at railway track transition zones. Soil Dyn Earthq Eng 2022;155:107200.
[16] Sun QD, Indraratna B, Nimbalkar S. Effect of cyclic loading frequency on the permanent deformation and degradation of railway ballast. Geotechnique 2014;64:746–51.
[17] Suiker ASJ, de Borst R. A numerical model for the cyclic deterioration of railway tracks. Int J Numer Methods Eng 2003;57:441–70.
[18] Vizcarra GC, Nimbalkar S, Casagrande M. Modeling behaviour of railway ballast in prismoidal apparatus using discrete element method. Proc Eng 2016;143:1177–84.
[19] Guo Y, Zhai W. Long-term prediction of track geometry degradation in high-speed vehicle–ballastless track system due to differential subgrade settlement. Soil Dyn Earthq Eng 2018;113:1–11.
[20] Dahlberg T. Some railroad settlement models - a critical review. Proc Inst Mech Eng F J Rail Rapid Transit 2001;215:289–300.
[21] Varandas JN, Hölscher P, Silva MAG. Settlement of ballasted track under traffic loading: application to transition zones. Proc Inst Mech Eng F J Rail Rapid Transit 2014;228:242–59.
[22] Nielsen JCO, Li X. Railway track geometry degradation due to differential settlement of ballast/subgrade – numerical prediction by an iterative procedure. J Sound Vib 2018;412:441–56.
[23] Yu Z, Connolly DP, Woodward PK, Laghrouche O. Settlement behaviour of hybrid asphalt-ballast railway tracks. Construct Build Mater 2019;208:808–17.
[24] Abadi T, Le Pen L, Zervos A, Powrie W. A review and evaluation of ballast settlement models using results from the Southampton railway testing facility (SRTF). Proc Eng 2016;143:999–1006.
[25] Liu J, Xiao J. Experimental study on the stability of railroad silt subgrade with increasing train speed. J Geotech Geoenviron Eng 2010;136:833–41.
[26] Ramos A, Gomes Correia A, Calçada R, Connolly DP. Ballastless railway track transition zones: An embankment to tunnel analysis. Transp Geotech 2022:100728.
[27] Shan Y, Zhou S, Wang B, Ho CL. Differential settlement prediction of ballasted tracks in bridge–embankment transition zones. J Geotech Geoenviron Eng 2020;146:04020075.
[28] Sayeed MA, Shahin MA. Design of ballasted railway track foundations using numerical modelling. Part I: Development1. Can Geotech J 2018;55:353–68.
[29] Li X, Department ME and JCON. Three-dimensional modelling of differential railway track settlement using a cycle domain constitutive model Xin. Int J Numer Anal Methods Geomech 2016;30:1303–36.
[30] Grossoni I, Powrie W, Zervos A, Bezin Y, Le Pen L. Modelling railway ballasted track settlement in vehicle-track interaction analysis. Transp Geotech 2021;26:100433.
[31] Zuada Coelho B, Varandas JN, Hijma MP, Zoeteman A. Towards network assessment of permanent railway track deformation. Transp Geotech 2021:29.
[32] Wolf JP, Deeks AJ. Foundation vibration analysis: a strength-of-materials approach. Choice Rev Online 2004;42. 42–0328–42–0328.
[33] Knothe K, Grassie SL. Modelling of railway track and vehicle/track interaction at high frequencies. J. Veh. Syst. Dyn. 1993;22(3–4):209–62.
[34] Connolly DP, Kouroussis G, Laghrouche O, Ho CL, Forde MC. Benchmarking railway vibrations - track, vehicle, ground and building effects. Construct Build Mater 2015;92:64–81.
[35] Lamprea-Pineda AC, Connolly DP, Hussein MFM. Beams on elastic foundations – a review of railway applications and solutions. Transp Geotech 2022;33:100696.
[36] Nielsen JCO, Igeland A. Vertical dynamic interaction between train and track—influence of wheel and track imperfections. J Sound Vib 1995;187:825–39.
[37] Nielsen JCO, Berggren E. Track geometry degradation and track stiffness on Swedish railway lines (Research report 2017:02). Gothenburg, Sweden: Department of Mechanics and Maritime Science, Chalmers University of Technology; 2017.
[38] Nielsen JCO, Berggren EG, Hammar A, Jansson F, Bolmsvik R. Degradation of railway track geometry – correlation between track stiffness gradient and differential settlement. Proc Inst Mech Eng F J Rail Rapid Transit 2020;234:108–19.
[39] Banimahd M. Advanced finite element modelling of coupled train-track systems: A geotechnical perspective (Ph.D. thesis). Edinburgh, Scotland: School of the Built Environment of Heriot-Watt University; 2008.
[40] Oscarsson J, Nielsen JCO. Dynamic train/track interaction with state-dependent track properties19. Gothenburg, Sweden: Chalmers University of Technology: Department of Solid Mechanics; 1999. Report F15.
[41] Nielsen JCO, Oscarsson J. Simulation of dynamic train-track interaction with state-dependent track properties. J Sound Vib 2004;275:515–32.
[42] Fermér M, Nielsen JCO. Vertical interaction between train and track with soft and stiff rail pads—full-scale experiments and theory. Proc Inst Mech Eng F J Rail Rapid Transit 1995;209:39–47.
[43] Nasrollahi K, Dijkstra J, Nielsen JCO, Ekh M. Long-term monitoring of settlements below a transition zone in a railway structure. In: 11th int symp on Field Monitoring in Geomechanics (ISFMG2022). 8; 2022. p. 147.
[44] Trafikverket. Ytvågsseismik (MASW) Gransjö, Boden. Project number, 100322. 2020.
[45] Varandas JN, Paixão A, Fortunato E, Zuada Coelho B, Hölscher P. Long-term deformation of railway tracks considering train-track interaction and non-linear resilient behaviour of aggregates – a 3D FEM implementation. Comput Geotech 2020;126:103712.
[46] Nielsen JCO. High-frequency vertical wheel-rail contact forces-validation of a prediction model by field testing. Wear 2008;265:1465–71.
[47] Andersson S, Söderberg A, Björklund S. Friction models for sliding dry, boundary and mixed lubricated contacts. Tribol Int 2007;40:580–7.
[48] Johansson A, Nielsen JCO, Bolmsvik R, Karlström A, Lundén R. Under sleeper pads-influence on dynamic train-track interaction. Wear 2008;265:1479–87.
[49] Nielsen JCO, Lombaert G, François S. A hybrid model for prediction of ground-borne vibration due to discrete wheel/rail irregularities. J Sound Vib 2015;345:103–20.
[50] Sällström JH, Åkesson BÅ. Fluid-conveying damped Rayleigh-Timoshenko beams in transverse vibration analyzed by use of an exact finite element part I: theory. J Fluids Struct 1990:561–72.
[51] Nielsen JCO, Abrahamsson TJS. Coupling of physical and modal components for analysis of moving non-linear dynamic systems on general beam structures. Int J Numer Methods Eng 1992;33:1843–59.
[52] Sällström JH, Åkesson BÅ. Fluid-conveying damped Rayleigh-Timoshenko beams in transverse vibration analyzed by use of an exact finite element part II: applications. J Fluids Struct 1990:573–82.
[53] Sato Y. Japanese studies on deterioration of ballasted track. Veh Syst Dyn 1995;24:197–208.
[54] Nasrollahi K, Nielsen JCO, Aggestam E, Dijkstra J, Ekh M. Prediction of differential track settlement in transition zones using a non-linear track model. In: Proc 27th Symp Inter Assoc Veh Syst Dynamics (IAVSD 2021); 2022.
[55] Getzner. Sylomer, Under Sleeper Pad SLB 2210 G. Report. 2023. n.d.
[56] Li X, Nielsen JCO, Pålsson BA. Simulation of track settlement in railway turnouts. Veh Syst Dyn 2014;52:421–39.
[57] Iwnicki S. Manchester benchmarks for rail vehicle simulation. Veh Syst Dyn 1998;30:295–313.